Simulation and Analysis of Morphing Blades applied to a Vertical Axis Wind Turbine

Robert Alexis Leonczuk Minetto

A thesis

in

The department

of

Mechanical, Industrial and Aerospace Engineering

Presented in Partial Fulfilment of the Requirements
For the Degree of
Master of Applied Science (Mechanical Engineering) at
Concordia University
Montreal, Quebec, Canada

November 2019

CONCORDIA UNIVERSITY

School of Graduate Studies

This is to certify that the thesis is prepared

By: Robert Alexis Leonczuk Minetto

Entitled: Simulation and Analysis of Morphing Blades applied to a Vertical Axis Winds Turbine

and submitted in partial fulfillment of the requirements for the degree of

Master of Applied Science in Mechanical Engineering

Complies with the regulations of this University and meets the accepted standards with respect to ordinality and quality.

Signed by the final examining committee:

_____ Chair

Dr. Georgios Vatistas

_____ Examiner

Dr. Mojtaba Kheiri

_____ Examiner

Dr. Bruno Lee

_____ Supervisor

Dr. Marius Paraschivoiu

Approved by _____

Dr. Georgios Vatistas

Chair of Department or Graduate Program Director

_____ 2019 _____

Dr. Amir Asif, Dean of Faculty

Gina Cody School of Engineering and Computer Science

ABSTRACT

Simulation and Analysis of Morphing Blades applied to a Vertical Axis Winds Turbine

Robert Alexis Leonczuk Minetto.

This study compares the performance of a Vertical Axis Wind Turbine with and without using morphing capabilities applied to its blades. It also explores the feasibility of applying moving mesh to model the morphing capability inside the software package STAR CCM+© in order to use Computational Fluid Dynamics (CFD) to analyze the flow's behavior. Particularly it is important to capture the presence of dynamic stall and vortex shedding at certain regions over the blade's path, which are associated with a decreased in the overall power coefficient. This work developed a methodology to analyze these morphing capabilities when applied over airfoils in 2D simulations, by using a combination of overset meshes and the morphing approach. The accuracy is verified by creating a baseline scenario and compare it against a benchmark case, while also testing for grid and time step sensitivity. The use of Reynold Averaged Navier Stokes equations was chosen, with Menter's SST k-omega as the turbulence model. Afterward, a maximum power coefficient curve was plotted by testing three airfoil's shapes as references, one forming the baseline case, while the other two delimiting the maximum deformation, marked as outward and inward cases. A final optimized case was tested, where the morphing was applied to strategic regions where the dynamic stall was highest, and where the shapes could ensure the maximum possible power output. This resulted in an improvement of 46.2% of the overall power coefficient.

ACKNOWLEDGEMENTS

First and foremost, I want to thank my supervisor Prof. Marius Paraschivoiu for his guidance along with this work, whose advice and patience I will always be thankful for. I want to thank my lab colleagues Leslie Taylor, Maria Zabarjad, Matin Komeili, and Jiyeon Lee, who were always there to offer support when needed, some academically, some professionally and some personally, and I am grateful to all of them for that.

I also want to thank my family, my parents Carlos and Adriana, my brother Emilio, my aunts and uncles, and my "Tía" Haydee, who will always be part of my family, I thank all of you for your unconditional love and support, which has helped me through these years. I am especially thankful to those friends who, even form the distance, send a message to just know about how you are doing, even after months between each talk, one will always appreciate their gesture. Friends like Matias, who has always supported me, been through longs talks or just by listening to me rambling about the day.

Finally, I want to thank the person that has made all this possible, the person whose support went far above and beyond what anyone could have asked for, whose care and company has saved me more than once and without whom I would not know where I would be today, the person I admire the most, Karen, I thank you.

The whole list of people I am thankful for, in one way or another, it is too big to convey on this page, from colleagues, co-workers, professors, and friends along these years, and even from before arriving in Canada, that I feel ashamed to not mention them all. To all of you, thank you for everything.

A special thank is given to the National Agency for Research and Innovation (ANII) from Uruguay for grant the necessary funds that made this study possible.

Contents

List of Figures

List of Tables

Nomenclature

Acronyms

VAWT Vertical Axis Wind Turbines

HAWT Horizontal Axis Wind Turbines

TSR Tipo Speed Ratio

CFD Computational Fluid Dynamics

RANS Reynolds Averaged Navier Stokes

PIV Particle Image Velocimetry

RBF Radial Basis Function

LES Large Eddy Simulations

DNS Direct Numerical Simulation

SST Shear Stress Transport

CFL Courant-Friedrichs-Lewy number

SSMA Synergetic Smart Morphing Aileron

Latin

P Power

Tor Torque

R Rotor's radius

V_∞ Free stream wind velocity

t Time

V Flow velocity (vector form)

m Mass

$\boldsymbol{F}$ Force

P Pressure

e Internal energy per unit mass

$\dot{q}$ Rate of heat transfer per unit mass

k Thermal conductivity

T Temperature

c_v Specific heat at constant volume

R_i Specific gas constant

S_{ij} Strain rate

k_t Turbulent kinetic energy

d_i Displacement distance

r_{ij} Magnitude of the distance between two vertices

x_i Position of the vertex

N Number of vertices

T_{ts} Turbulent time scale

$\bar{V}$ Mean velocity

f_{beta^*} Free shear modification factor

f_{beta} Vortex stretching modification factor

G_k Turbulent production

G_{nl} Nonlinear production

G_b Buoyancy production

G_ω Specific dissipation production

D_ω Cross-diffusion term

F_1 Blending function

d Distance to the wall

$CD_{k\omega}$ Cross-diffusion coefficient

S Modulus of the mean strain rate tensor

$f^{pressure}$ Pressure vector

f^{shear} Shear force vector

n_f User-specified direction vector

p_f Face static pressure

$\dot{m}$ Mass flux

p_{ref} Reference pressure

T_f Stress tensor over the surface

F_x X force component

F_y Y force component

F_N Normal force

F_T Tangential force

C_L Lift coefficient

C_D Drag coefficient

C_P Power coefficient

C blade's chord length

V_{rel} relative velocity

y normal distance from the wall-cell centroid

u* reference velocity

L lift

D drag

i incidence angle

Greek

ω angular velocity

ρ density

τ_{ij} Stress components

μ dynamic viscosity

λ bulk viscosity

μ_t eddy viscosity

δ_{ij} Kronecker delta

β_i proportionality factor.

λ_j expansion coefficient

ν kinematic viscosity

τ_w wall shear stress

α_i interpolation weighting factors

$\phi_{acceptor}$ variable of interest on the acceptor cell

ϕ_i value of the dependent variable at the donor cells

$\boldsymbol{a}_f$ face area vector

θ azimuthal angle

α angle of attack

ρ_∞ free stream density

1. Introduction

This chapter presents a brief introduction to Vertical Axis Wind Turbines (VAWT), along with the motivations, objectives, and contributions behind this work. It starts with a quick presentation about the current world's energy needs and then makes a comparison with Uruguay's current energy matrix. which has seen exponential growth in its wind power capacity in recent years. A short discussion about wind turbines, in general, is mention along with their types, benefits, and challenges, especially surrounding VAWT. Finally, the dissertation's outline is presented.

1.1. Overview

Over the last decades, there has been an increased interest worldwide to make a transition from energy matrices that relied heavily on fossil fuels to more sustainable and focus on low-carbon emission type of energy sources [1]. This presents many opportunities and challenges for the research community to explore, from generation, transmission, distribution, logistics, manufacturing, consumer end services, etc., inside this spectrum of possible solutions, we choose to focus on wind energy generation. Its power capacity has grown significantly around the world over the last decades as seen in Figure 1 [2], with countries like Uruguay adopting it as an integral part of its electrical grid by having as of January/2018 as much as 44% of its monthly electrical generation coming from wind sources with a small percentage from solar power [3]. This reduces the country's dependence on fossil fuels to supply for its thermoelectric power plants, as well as lowering electricity imports from neighboring countries [4].

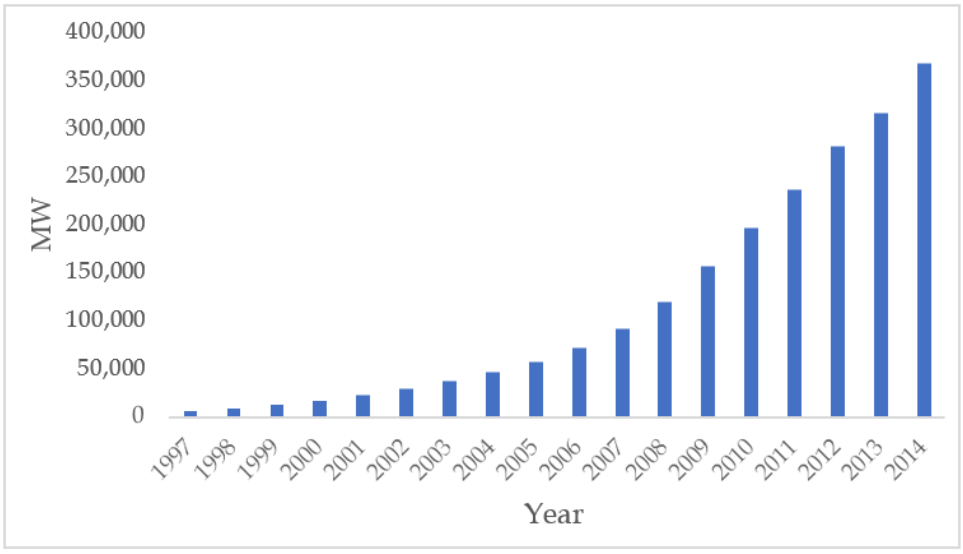

Figure 1 - World's cumulative installed wind power capacity from 1997-2014 [2].

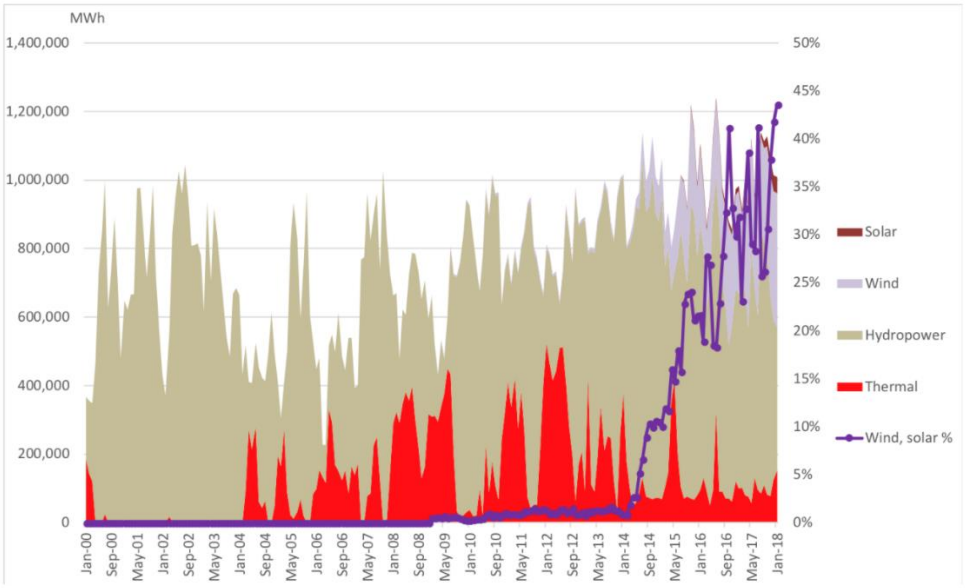

Figure 2 - Uruguay's electrical generation sources from 2000-2018 [3].

Examples like this should serve as a case study for other countries as such endeavors make the nation less dependent on fossil fuels, and in some cases as in Uruguay, less dependent on energy imports as mentioned above. Besides the political/economic benefits from an energy independent state, in the long run, this shift from energy sources helps by mitigating the emission

of future greenhouse gases associated with burning fossil fuels. These gases had been associated with increased temperatures on the planet and great efforts are put to understand its impacts, following this logic, it seems imperative to look forward to ways to reduce their emissions [5].

1.2. Wind power

Wind turbines have been commonly used to generate electricity by harvesting the power of the wind. There exist several categories of wind turbines that are distinguished by their type, like depending on size, power capacity, the position of the rotational axis, main aerodynamic forces that drive it (lift or drag based), and so on. Take for example the position of its axis of rotation, where we can divide between horizontal and vertical axis wind turbine, HAWT and VAWT according to their respective acronyms, where their axis is located parallel or perpendicular to the general wind direction. Examples of both types can be seen below in Figures 3-4.

Figure 3- Example of Horizontal Axis Wind Turbines (HAWT) located in Maldonado, Uruguay [6].

Figure 4- Example of Vertical Axis Wind Turbine (VAWT) located in Alberta, Canada. Extracted from [7]

In general, HAWT have been preferred over VAWT because they usually have an average of 16% higher power output than VAWT [8], this can be observed in Figure 5, where the power coefficient is plotted against the Tip Speed Ratio (TSR) between different wind turbines is shown.

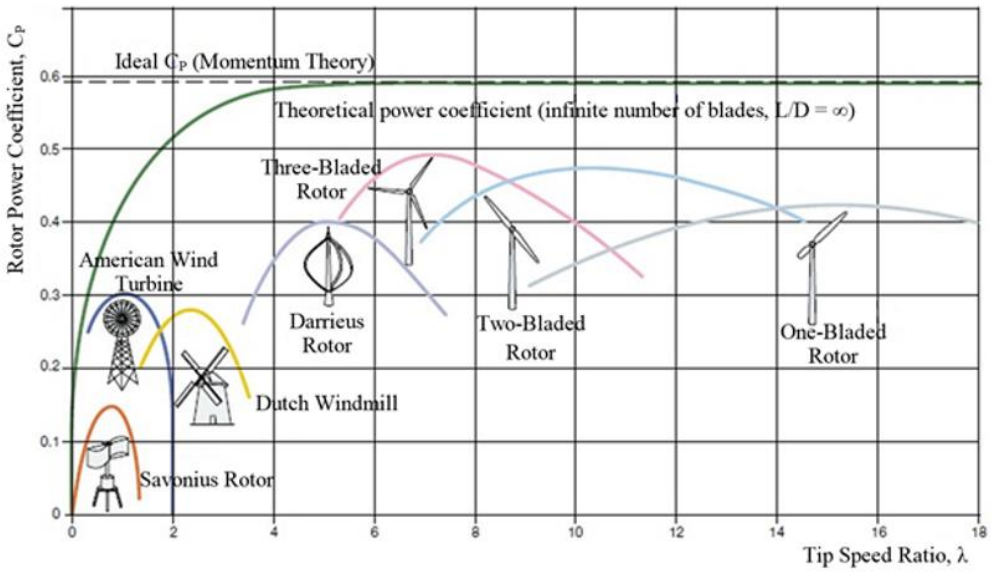

Figure 5- Power coefficient comparison for different wind turbines models. Extracted from [9]

Power coefficient is defined as the harnessed power by the turbine to the kinetic energy that is available in the wind, which mathematically can be translated to:

$$Cp = \frac{P}{0.5\rho_\infty A_s V_\infty^3} \tag{1.1}$$

Where P is the turbine's power, ρ_∞ is the free stream density, A_s is the rotor's swept area and V_∞ is the free stream velocity. The turbine's power can be measured to be equal to the torque (Tor) imposed on the rotor by the wind times the angular velocity ω.

$$P = Tor\omega \tag{1.2}$$

The TSR is the ratio between the turbine's blade velocity at its tip over the free stream velocity of the wind.

$$TSR = \frac{R\omega}{V_\infty} \tag{1.3}$$

Where R is the rotor's radius, ω is the rotor's angular velocity and V_∞ is the free-stream wind velocity. From Figure 5 the maximum power coefficient is higher for some HAWT models when compared to VAWT, with the possibility to operate on a broader range of wind speeds. It can also be stated that theoretically, a wind turbine's power coefficient is restricted to a maximum value of 0.593 according to Betz's law [10].

Even though HAWT have a higher power output, they have some disadvantages that should be considered, for example, they tend to be noisier than their VAWT counterparts, as well as suffer from a higher dependency on the wind's direction, and their powerhouses are located at an elevated position(inside the nacelle) which makes maintenance more difficult [8,9]. In the case of VAWT, they usually work independently from the general wind's direction, the powerhouse is commonly located at ground level which facilitates maintenance and they tend to produce less noise [8,9].

1.3. Motivation

Knowing that VAWT have several advantages over HAWT, yet they lack the same power output, served as a motivation for this work as they could function on places where lower wind speeds are more dominant like near cities, or at the top of buildings where having the powerhouse located at the roof instead of an elevated nacelle could be safer. Regarding the power output, there are several approaches that can be applied to VAWT to improve it. As it will be shown along with this work, a VAWT deals with a complex flow behavior as the blades rotate. They generate vortexes that shed downstream decreasing the overall power output by lowering the lift generated by the blades. It could also happen that the vortexes could collide with the rest of the blades in its wake, further decreasing the power output [11].

In the literature an approach was found to aid on this issue, by deforming the airfoil itself, changing its shape during certain periods of the rotation could reduce or delay the flow's detachment, increasing the power coefficient experienced. This approach was explored by Secanell *et al.* [12] using aerodynamic shape optimization, Kerho [13] using adaptative airfoil design, and Hefeng *et al.* [14] who later showed that flexible airfoils could experience better lift capabilities by reducing the flow's detachment. Traditionally, one could use control surfaces attached to the airfoil like flaps to change the flow's path around it in a way to improve lift capabilities [15]. Pankonien *et al*. [16] at the University of Michigan designed an airfoil which is capable of deforming itself by integration the actuation mechanism inside the airfoil itself, they call this as a Synergetic Smart Morphing Aileron (SSMA) which uses composite materials as internal actuators to shape its surfaces, particularly near the leading edge. The advantage of this approach is that it allows for a continuous surface over the blade as it deforms, avoiding

discontinuities commonly found on traditional control surfaces (like flaps) that can trigger flow separation.

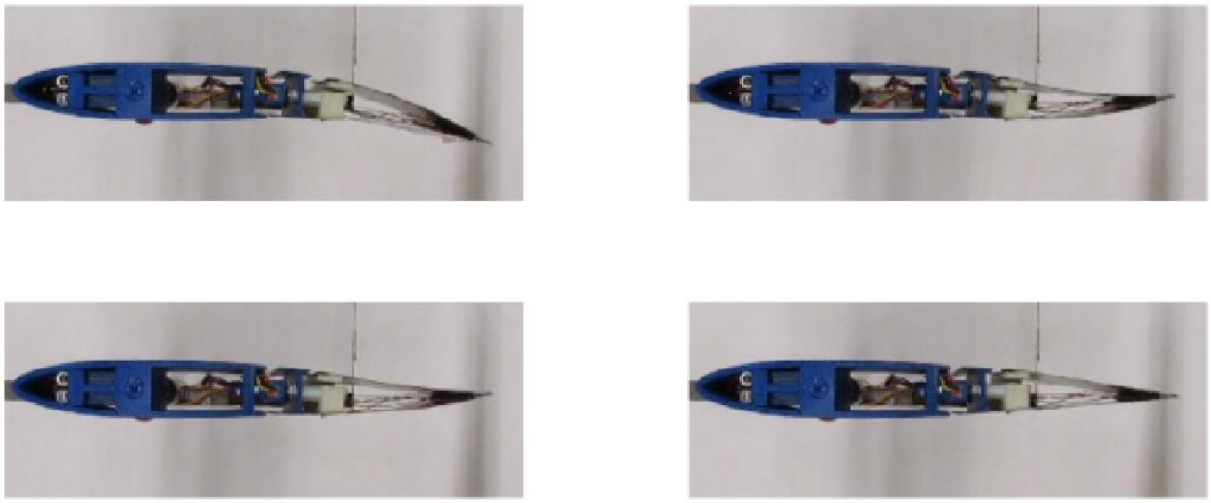

Figure 6 - The Synergetic Smart Morphing Aileron (SSMA) designed by Pankonien et al [16] and its possible configurations.

1.4. Objectives

This work intends to compare the performance of a VAWT with and without using morphing capabilities and to explore the feasibility of applying the latter inside the software package STAR CCM+© in order to use Computational Fluid Dynamics (CFD) to create simulations to analyze different scenarios. In order to do this, it is necessary to:

- Develop a methodology that allows us to use both rotating and deforming techniques simultaneously.
- Validate the methodology by creating a simulation to serve as the baseline case, then back it with experimental data found in the literature for similar cases.

- Compare the baseline case applying only rotational motion against one with the morphing capabilities activated over several regions along the VAWT path.

1.5. Contributions

This work developed and tested a methodology to analyze morphing capabilities applied over airfoils in 2D simulations to study its influence on VAWT's performance by using the software package offered by STAR CCM+©. The morphing was applied in strategic regions where the dynamic stall was highest over the turbine's path, resulting in an improvement in the overall power coefficient.

1.6. Dissertation's outline

This dissertation has been structured as follows: Chapter 2 covers a review of the theory surrounding the aerodynamics aspects of VAWT, the dynamic stall, vortex shedding and an introduction to mesh techniques related to simulating rotational and morphing movements. Chapter 3 expands on the equations and numerical methods involving the RANS equations, boundary layer theory, discretization schemes, and the k-omega turbulence model. Chapter 4 addresses the validation portion of this study, where grid and time step sensitivity studies were done as well as a comparison between the results obtained from a prepared baseline scenario against other CFD cases and experimental data. Chapter 5 presents the major portion of results obtained along with this work, parting from a base VAWT model and adding morphing capabilities later. Finally, Chapter 6 reports the conclusions derived from this study, as well as leaving the final considerations and suggestions for future work.

2. Literature review

2.1. Aerodynamic considerations

There are several types Vertical Axis Wind Turbines (VAWT): turbines that are drag force based usually shared similarities with the Savonius type of turbine and turbines that are lift based such as the Darrieus and H-rotor (also known as H-Darrieus rotor) [9], Figure 7 shows some examples of these designs.

For this study, we choose to focus on an H-rotor type turbine, as they tend to experience higher power coefficients than the Savonius one, although the latter has better self-starting capabilities because the H-rotor commonly uses symmetrical airfoils, which tend to perform poorly in this matter [17]. At this stage of the research, we consider that the power output necessity outweighs the needs for a better self-starting and that this issue should be left for future work. Furthermore, between the Darrieus and H-rotor type, the latter is preferred as it deals with a much simpler geometry, which would translate into cheaper manufacture for future projects.

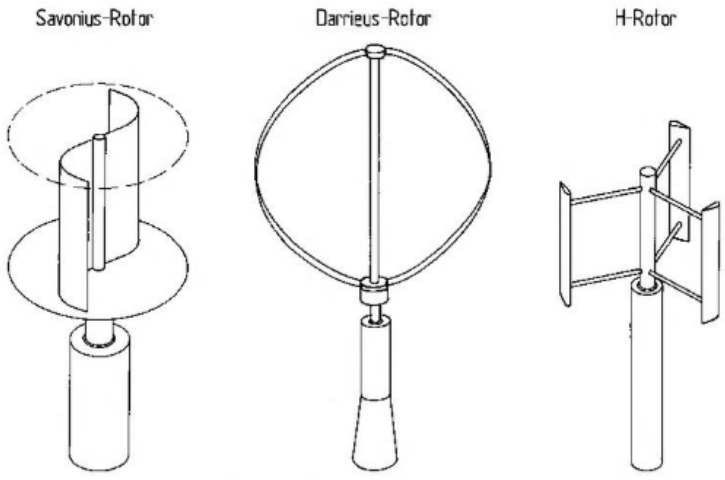

Figure 7- Types of VAWT [9].

2.2. Dynamic stall and vortex shedding.

Although the H-rotor requires a simpler geometry, the flow's behavior as it passes through it is still quite complex, particularly when a phenomenon like dynamic stall and vortex shedding start to develop and affect the overall turbine's performance [11]. The dynamic stall is due to the blade's rotational motion, changing continually its angle of attack as it goes through the cycles, this causes an unsteady pitch-like movement as seen by the blades [18]. This angle of attack is not only dependent on the azimuthal position (where the blade is located relative to the axis), but also on the free stream velocity and the velocity of the blade, as these two combined forms a relative velocity that seen by the airfoil, determines the relative angle of attack that it is experiencing as seen on Figure 8. This can be expressed as an equation using the TSR as follows [19]:

$$\alpha = \text{atan}\left(\frac{sin(\theta)}{cos(\theta) + TSR}\right) \tag{2.1}$$

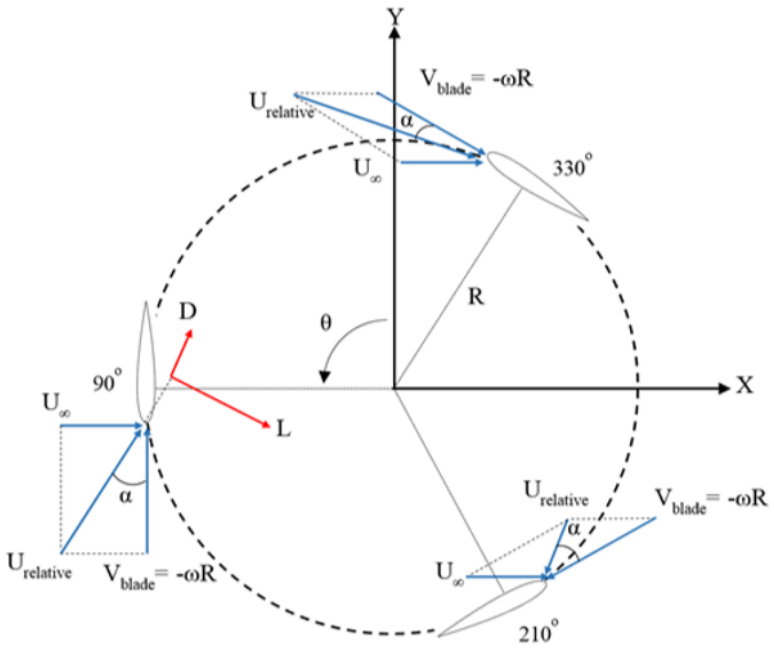

Figure 8- Velocities relations and resultant effective angle of attack for H-rotor type turbine [9].

Figure 9 is a representation of plotting Equation 2.1 by using several TSR values, here it can be seen how the angle of attack changes through the whole cycle, and that for lower TSR values the change is greater reaching asymptotic behavior at TSR=1.

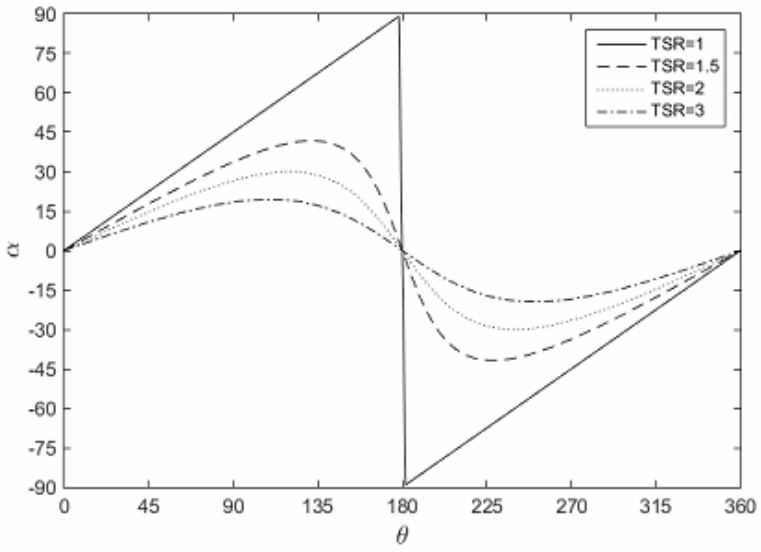

Figure 9 -Relation between the angle of attack with the azimuthal angle for several TSR values.

The relation between dynamic stall and the effective angle of attack is better understood when we think about static stall first, a more common phenomenon. Take an airfoil placed within a moving flow, the interaction between the two will result in the lift being generated with an associated angle of attack. As we move the airfoil in a pitch-motion, increasing the angle of attack the lift also increases almost linearly for low and moderate angles as it is shown in Figure 10(a), where the lift is expressed as a coefficient rather than a dimensional variable. At this stage the flow tends to move smoothly around the airfoil, but as we continue to increase the angle of attack a turbulent region starts to form near the leading edge of the airfoil, an adverse pressure gradient also appears and eventually flow separation starts to happen [20], this transition can be seen on Figure 10 (b).

If the increase in the angle of attack continues even further, the flow separation intensifies, a sudden drop in the lift appears and large vortexes are produced, this is known as the stall point [15]. In the case of dynamic stall, because it is a cycle the lift coefficient plot is represented by a hysteresis curve that can be used to compare against the static stall as seen in Figure 11. For low angles of attack, both curves share approximate coefficients, but the static stall point is reached before the dynamic one, although both seem to drop to the same values approximately.

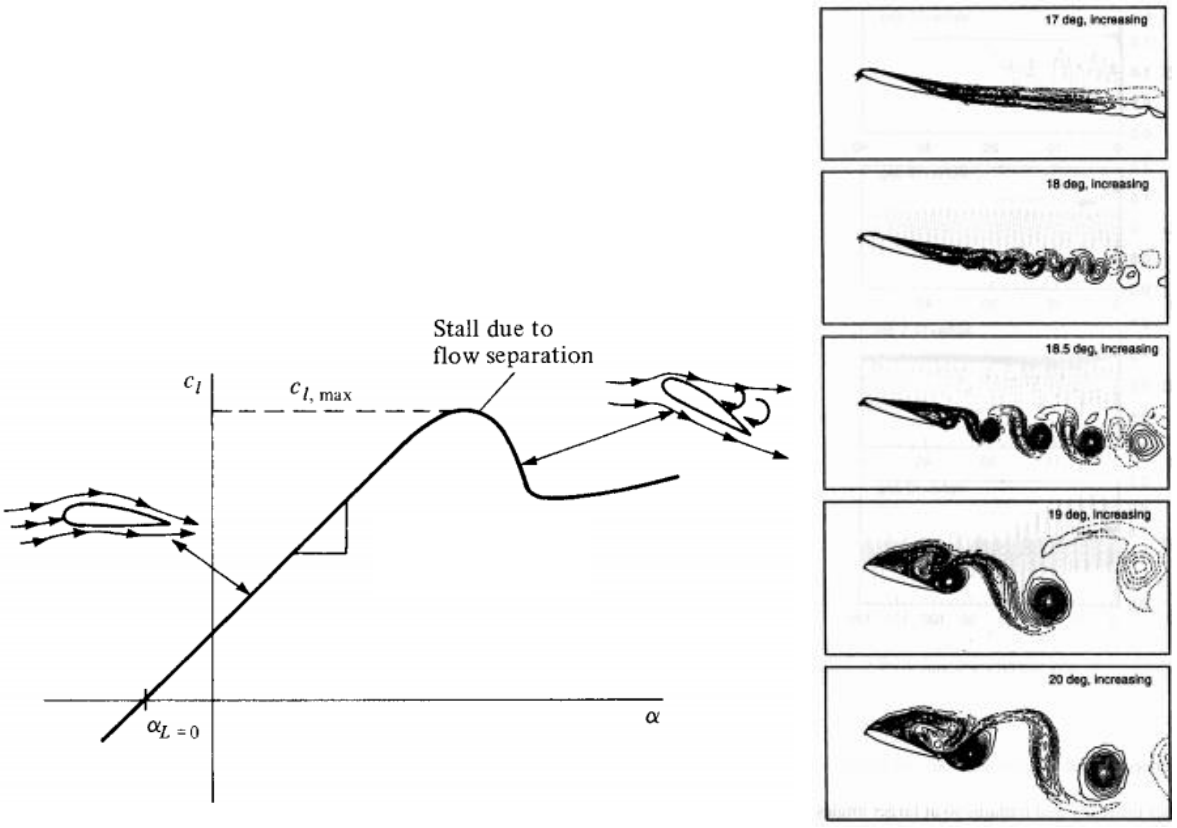

(a) (b)

Figure 10- (a) Plot of lift coefficient variation with respect to the angle of attack. Modify it from [15]. (b) Vorticity field for various angles of attack using a NACA 0012 airfoil inside turbulent flow with Re= 10^6 [20].

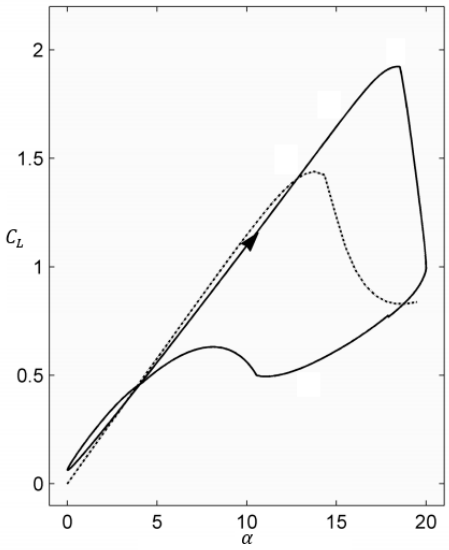

Figure 11- Comparison between static stall (dotted line) vs dynamic stall (solid line). Modified from [21].

Several studies have been done in order to understand dynamic stall and its causes, for example McCroskey *et al.* [22, 23] points out that the unsteady change in the angle of attack derived from the rotation of the airfoil (as shown in Figure 9) can cause the separation of the turbulent boundary layer, here dynamic stall was studied using wind tunnel experiments on NACA 0012 airfoils. This was also confirmed by Mullernes *et al* [24], and Lee *et al.* [25] which tested it on oscillating NACA 0012 airfoils by using particle image velocimetry (PIV) and hot-film sensor arrays respectively. Because of its complexity, there are several factors that seem related to dynamic stall, Ferreira *et al.* [26] developed a methodology to study the formation of dynamic stall on NACA0015 airfoils by using PIV and comparing several CFD turbulence models for low TSR. Later Ferreira *et al.* [27] pointed out that dynamic stall seems to be related with the development of two regions over surface where a pair of vortexes are generated, near the leading and trailing edge respectively, rotating in opposite directions and shedding downstream afterwards this can be seen on Figure 12 where vorticity contours are shown.

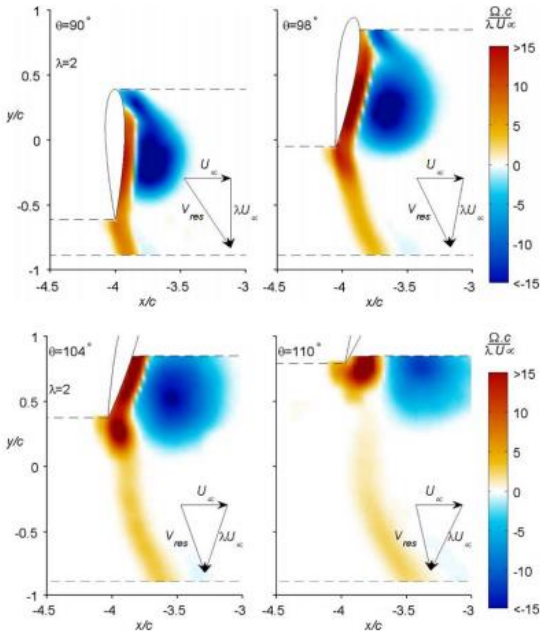

Figure 12- Vorticity contour plots showing the development of the two vortex regions at the leading and trailing edge [27].

Corcos *et al*. [28] studied and identified this roll up the behavior of the vortexes over the airfoil, and Fujisawa *et al.* [29] confirm the existences and development of these vortexes over the airfoil during dynamic stall by presenting images captured by using PIV(see Figure 13).

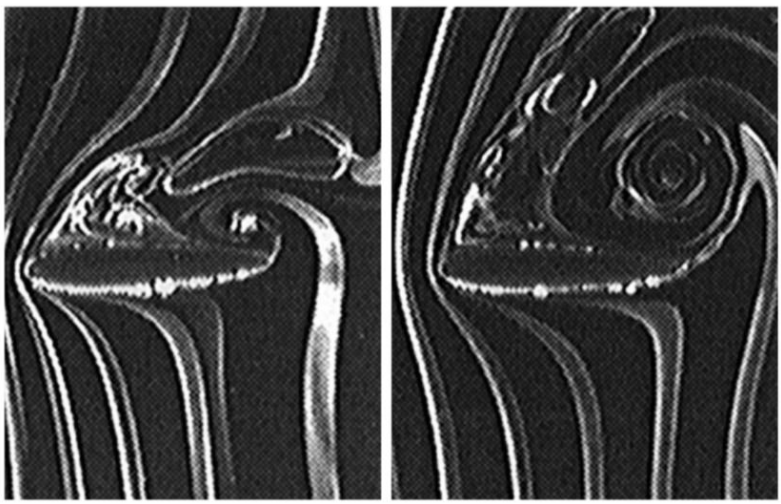

Figure 13- Images gather by Particle Image Velocimetry(PIV) showing vortex roll up over an airfoil [29].

The shape of an airfoil is strongly related to the resultant aerodynamic forces that it will experience, for our case a quasi-symmetrical airfoil will be used which resembles the "non-morphed" state of the SSMA airfoil shown on the bottom right picture in Figure 6, this approximates almost to a NACA0012 profile. This dependence on the airfoil's shape is going to be useful along with this work, as we will focus on how to deform the airfoil's shape during its path to improve its power coefficient by dealing with the dynamic stall. Here the hypothesis will be that by deforming the airfoil we can change the point where flow separation will occur and subsequently, we can have control to a certain degree over the dynamic stall, hopefully reducing it and by doing so improving the overall power output of the turbine.

Another important variable to consider is the Reynolds number, as it relates a handful of flow properties and helps characterize the flow. Choudhry et al. [30] studied the influence on the mean Reynolds number over the dynamic stall, they point out that an increase on it appears to be related to a delayed in the detachment of the boundary layer, and consequently delaying the vortex shedding. The apparent reason behind this seems to be that larger Reynolds number will carry higher inertial forces that would help overcome the adverse pressure gradient over the airfoil, therefore delaying the flow separation. One thing to notice is that because of the continues change on the relative velocity as "felt" by the airfoil, the local Reynolds Number will also change constantly around the blade's path, and by this the airfoil will experience higher and lower local Reynolds numbers than the mean free stream depending on where it is located. As an example, as the TSR values tend to 1, the local Reynolds number tends to 0 for the azimuthal angle at 0 degrees as explained by Scheurich [31], because the relative velocity seen by the flow near the airfoil's surface at that point would be close to zero.

Another issue related to dynamics stall is that not only causes a drop in the lift generated as the vortexes develop and detach from the airfoil, but also afterward as these vortexes shed downstream, they could collide with other blades as studied by Amet *et al.* [11], disrupting the flow around them and causing an even further decrease on the power coefficient. Figure 14 shows a diagram with examples of possible paths for the vortexes as the shed downstream at TSR=2 [11].

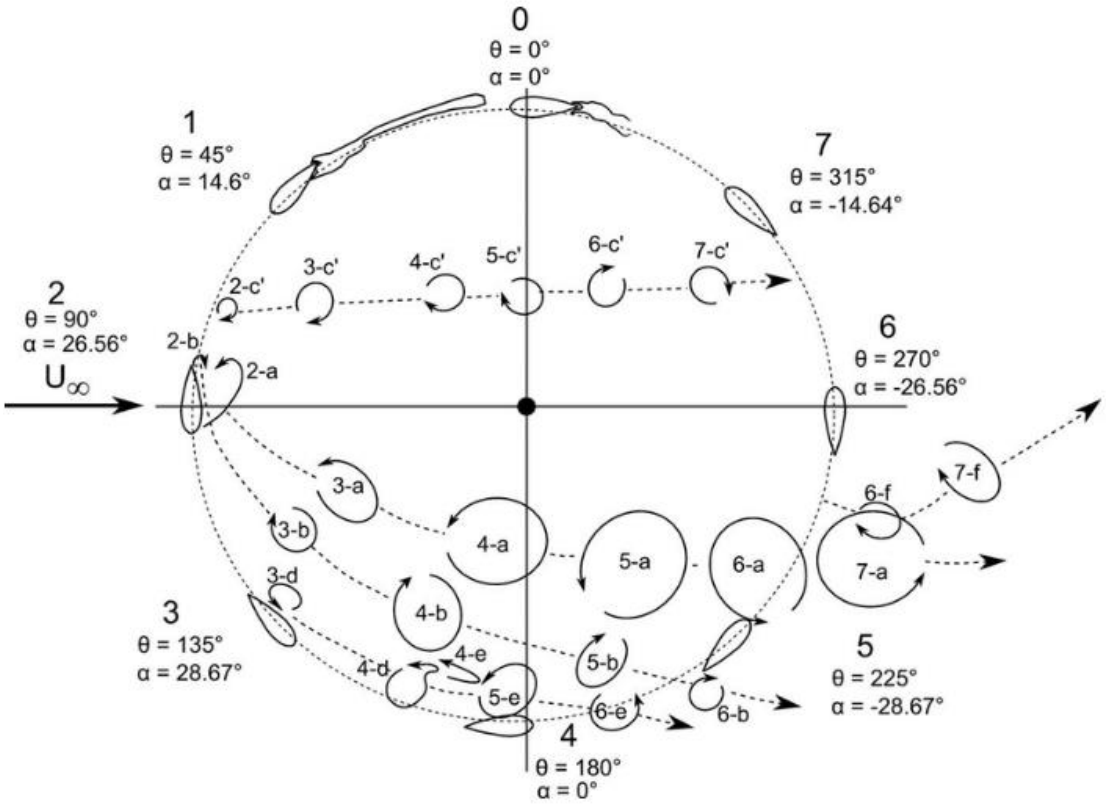

Figure 14- Possible paths for vortex shedding in a Darrieus turbine operating at TSR=2 [11].

2.3. Dynamic Mesh Methods

In simple terms, dynamic meshes methods refer to a group of techniques that allow us to change the position of mesh points during a simulation, which is needed to simulate the rotation

of the blades from a turbine or a fan or the translation motion of a piston inside a cylinder [32]. The two main approaches to do this are: 1) Re-meshing, here the connectivity of the mesh is changed at each step or number of steps, or 2) Simply by moving the vertices/ mesh points around the domain, re-meshing can guarantee better mesh quality at the end of each cycle, but it is more expensive to run [33]. Along with this work, we will demonstrate that simple mesh deformation without remeshing is enough for our case by showing that mesh quality is sufficiently conserved to the point of not needing to re-meshing, this will speed the simulations considerably as each cycle will require several deformation steps.

Now regarding the vertex points when moving the mesh, one must account for how the movement it is going to be done, if it happens in one step the "jump" in space could be too large and the solution could become too unstable to the point of diverging as the experience in this work has shown, the reason for this will be explained in more details on chapter 3. To solve this issue, one can increase the number of steps between the initial and final position, effectively "smoothing" the transition between both, but the rate and how these steps are taken needs to be regulated by a set of rules. Some smoothing techniques use the spring equation, the Laplace equation or Radial Basis Functions to do it for example.

The equation spring smoothing technique as proposed by Batina [34], consists in using the Hooke's law and apply it to each grid point on the mesh, this creates a pseudo physical system of springs with a total force over it equal to 0, Figure 15 shows a sketch representing the spring method as an analogy with actual springs. When we purposely choose to move some mesh points to a new position, the systems become unstable and it starts to compensate it by "dragging" neighboring points with it until it reaches a new stable position at the end of the movement. This technique has been improved by Blom [35] by adding a power coefficient inside the stiffness

calculation and has been described to show good results for linear types of motion, like the translation from a piston. This technique seems to have issues with more complex types of movements [36]. Because of this, more robust versions of the spring method have been developed like using torsional springs as proposed by Fahat et al. [37], or the ball-vertex method proposed by Bottaso et al. [38].

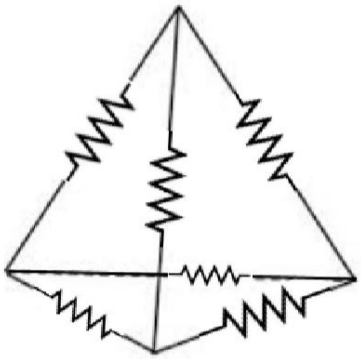

Figure 15- Representation of the spring analogy [33].

The Laplace equation approach or also known as the diffusion method, applies as its name indicates the Laplace equation to smooth an imparted movement over the mesh, the surrounding area will perceive the said movement by its diffusion factor and will move other neighboring points according to the distance to the point where the movement began as proposed by Lohner et al. [39]. Hsu et al. [40] argue that a disadvantage of using the Laplace equation is that when the new positions for the points are solved, it is done independently of each other, therefore only accounting for their distance to the point where the movement began, but not the relation with each other, this could carry issues with certain type of motion like translation over only one direction.

There are more sophisticated techniques to obtain a smooth transition and maintain a high-quality grid, for example, the Radial Basis Function interpolation created by Boer *et al.* [41], calculates the displacement of the interior nodes on the grid by using an interpolation function based on the displacement of the nearest wall. This technique was successfully tested by Bos *et al.* [42] when applied to deform a mesh representing an airplane's wing and conserving a high-quality mesh by the end of the motion. Boer et al. [41] also demonstrated that the RBF method maintains good orthogonality on the grid near the moving boundaries, which translates to a higher quality mesh. Tan [43] realized a comparison by reviewing several smoothing techniques and concluded that RBF results to be the more robust method, but also the most expensive in terms of computational cost. As such studies have been made in order to speed up the process, Su et al. [44] suggested that the use of a Greedy algorithm could reduce the computational cost while been robust to handle complex rotor configurations.

With this we have the set of tools needed to accomplish the deformation movements required by the airfoil, now let's consider the rotational motion that it is needed to make the airfoil/blade behaved like an actual turbine. Usually, this kind of movement is simple to represent, and software packages like STAR CCM+ © deal quite well with such movements by offering features like applying solid body rotation or a moving frame of reference for the inlets [45]. Note that as we are rotating a segment of the whole domain, some grid points will be forced to change its connectivity as they move further away during the rotating steps. To deal with this issue, we can choose to implement a sliding mesh technique, where the defined rotating zone containing the airfoil will move as a solid object while the grid points over its boundary (between the rotating region and the static one) exchange information by interpolation between the cells

[45]. The advantage of this technique is that is relatively cheap to process, as the interpolation only occurs over a layer of adjacent cells over the boundary between the two regions. [45]

The other option is to use overset meshes where two regions at least are required to be defined, a static (background or underset mesh) and in our case a rotational one (Overset-mesh) which could involve other types of motion as well. The two meshes are stack one over the other, and then the superpose part of the background mesh is cut out in a process called "hole cutting" [45]. This removes almost all of the background mesh grid points in the area except for the boundary between the two meshes, here an interface is created where for the two meshes coexist and allows them to communicate via interpolation according to the STAR CCM+© manual [45], Figure 16 shows an example of an overset mesh before and after the "hole cutting" process is applied. The interpolation process will be explained in more detail in chapter 3.

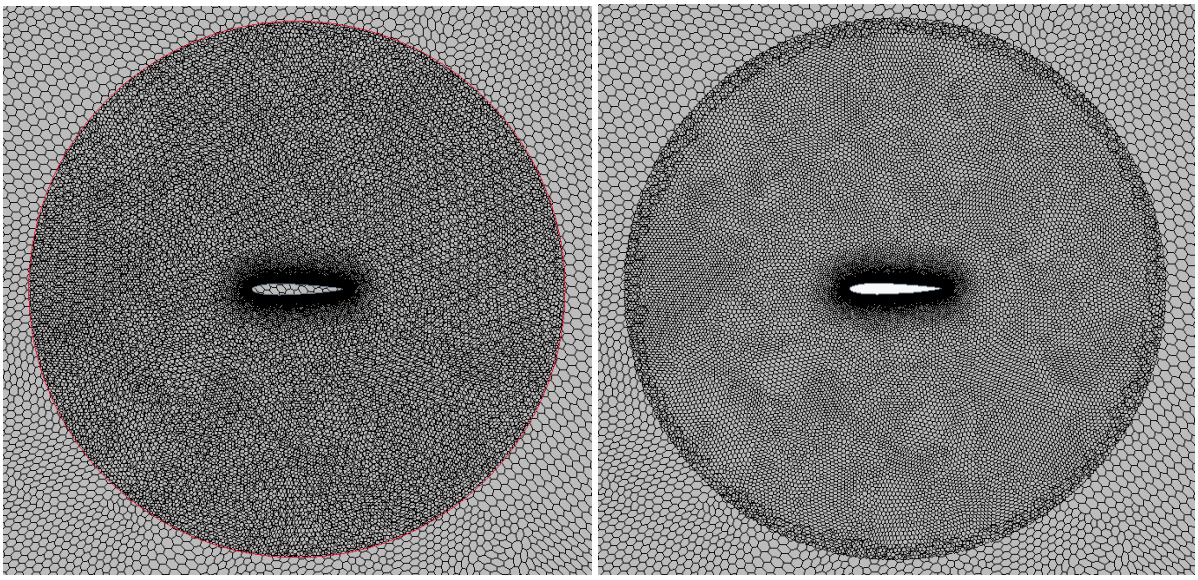

Figure 16- Before and after "hole cutting" process is initialized over an overset mesh inside STAR CCM+©.

For this study we choose to use overset meshes over sliding meshes, even though they are more expensive than the latter because STAR CCM+© at the current version available for this work (12.06.011), only allows the simultaneous use of morphing techniques (deforming the airfoil) with the overset mesh (rotating aspect) and not with the sliding mesh feature [45].

2.4. Turbulence modeling

Once the methods associated with resolving the mesh movements are finally chosen, it is time to set up the turbulence model. As we work with computational fluid dynamics (CFD) we try to work around a way to discretize the conservation equations of mass, momentum, and energy with a series of assumptions and numerical models. According to Taylor [46], there is not an agreement between the CFD community on what is the correct method to use in order to simulate the dynamic stall and the vortexes that derive from it in a VAWT. Taylor [46] also argues that because of its relatively inexpensive cost, the Reynolds Averaged Navier Stokes equations approach seems more favorable to be used for commercial purposes, at least when compared to heavier models like Large Eddy Simulations (LES) or Direct Numerical Simulation (DNS). It is worth to point out that as computational power has become more accessible and cheaper, there has been a rapid increase over the last decade in research and industry on the application of LES based simulations [48], and even DNS studies to some extent [49], although mainly dedicated to fundamental studies(using low Reynolds number) or calibration of other models[50-51].

Figure 17 shows a sketch with a quite simplified comparison between RANS, LES and DNS and their relation between how much is resolved vs how much is modeled with each approach [51] taking the sizes of the eddies as the main variable. This is because eddies are useful to represent the scale of details in our flow, as we can observe from the largest eddies that would

transfer turbulent kinetic energy from the mean flow into smaller eddies, all the way down to the Kolmogorov scale with the smallest eddies where the energy is transfer by heat dissipation [52].

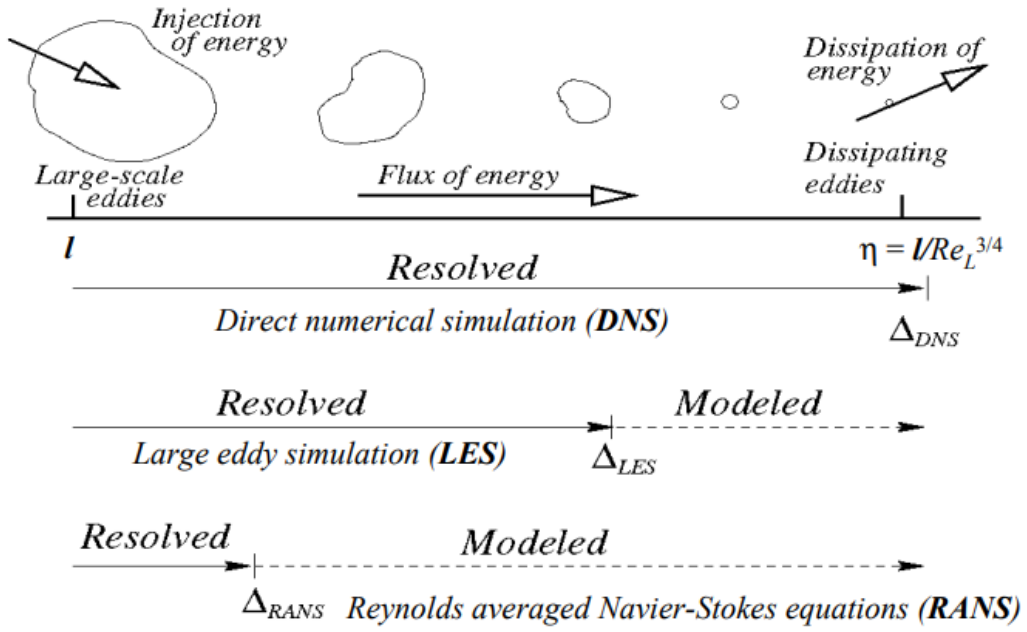

Figure 17- Simplified sketch comparing the degree of modeling required between RANS, LES and DNS [51].

There are several ways to model turbulence by using a RANS model, depending on the number of equations used, this could be a zero-equation model(mixing length model), one equation (Spalart-Allmaras), two-equation models (k-ε and k-ω models with their variants), or seven equations (Reynolds stress model) [52]. Both Tan [44] and McLean [53] have studied VAWT performing simulations using CFD and suggest that the SST k-ω model was appropriate as it obtained reasonable accuracy with a moderate computational cost. As such, for the purpose of this study, we chose to use the SST k-ω model as well. The equations behind this turbulence model will be explored in more detail in Chapter 3.

3. Numerical modeling

Up to this point, we have introduced what vertical axes wind turbines are, their types and characteristics, including some of their benefits and challenges, such as dealing with dynamic stall and vortex shedding. Some ideas have risen over the years to control these issues, like the SSMA system in order to deform the airfoil, adapting its shape with the goal to mitigate these effects that decrease the power output of the turbine considered. To understand how this works. it is necessary to pay attention to what's happening to the flow as it moves around the turbine. As experimental setups can be prohibitory expensive to do, one can rely on CFD techniques to analyze the flow and capture its features with reasonable confidence. In this chapter we are going to explore the theories behind how CFD is used to simulate the flow, this will be by introducing the conservation equations, their limitations, the assumptions needed to use them, and what models to use in order to close the problem so it can solve on a computer. It is also discussed the problems related to the deforming airfoil that was introduced in chapter 2, and the techniques available to solve it, like the use of overset meshes and the spring model/basis functions while using a commercial CFD package like STAR-CCM+©.

3.1. Governing equations

In fluid mechanics, there is a group of fundamental equations that helps us understand and represent a fluid's behavior by accounting for the conservation of mass, momentum, and energy-related to that system. Although these equations represent the foundation for fluid mechanics and consequently for CFD methods, it is not possible to fully solve them analytically therefore simplifying assumptions is needed. This requires the creation of models and the

introduction of new equations in order to close and solve the system, some of those are explained in this chapter.

3.2. Conservation of mass

When we consider a finite control volume filled with a fluid and stated that the mass must be constant in it, this is, the mass can neither be created nor destroyed over the closed system, the conservation of mass can be express as a partial differential equation (known as the continuity equation) with the form:

$$\frac{\partial \rho}{\partial t} + \nabla.(\rho \mathbf{V}) = 0 \tag{3.1}$$

Where ρ is density, t is time, and $\mathbf{V}$ is the flow velocity in vector form, this equation relates the flow variables to a given point for a three dimensional, unsteady, compressible and viscous flow.

3.3. Conservation of momentum

To talk about the second fundamental equation, first, it is needed to remember Newton's second law where force is equal to the time rate of change of momentum (m.V).

$$\boldsymbol{F} = \frac{d}{dt}(m\boldsymbol{V}) \tag{3.2}$$

When this is applied to a finite control volume, considering all surface forces that interact with the flow and its boundaries for a three dimensional, unsteady, compressible and viscous case, the total force experienced by the fluid can be expressed as:

$$\rho \frac{Du}{Dt} = -\frac{\partial p}{\partial x} + \frac{\partial \tau_{xx}}{\partial x} + \frac{\partial \tau_{yx}}{\partial y} + \frac{\partial \tau_{zx}}{\partial z} \tag{3.3}$$

$$\rho \frac{Dv}{Dt} = -\frac{\partial p}{\partial y} + \frac{\partial \tau_{xy}}{\partial x} + \frac{\partial \tau_{yy}}{\partial y} + \frac{\partial \tau_{zy}}{\partial z} \tag{3.4}$$

$$\rho \frac{Dw}{Dt} = -\frac{\partial p}{\partial z} + \frac{\partial \tau_{xz}}{\partial x} + \frac{\partial \tau_{yz}}{\partial y} + \frac{\partial \tau_{zz}}{\partial z} \tag{3.5}$$

Where p is pressure and $\frac{Du}{Dt} = a_x$ is the x component of the acceleration experienced by the flow as the substantial derivative of u component of velocity, this is also analogous to $\frac{Dv}{Dt} = a_y$ and $\frac{Dw}{Dt} = a_z$ as the acceleration y and z components in a cartesian coordinate system respectively. The substantial derivative can be decomposed as shown below, where the first term on the left side is can be interpreted as a local derivative dependent on time and the second term as a convective derivative.

$$\frac{D}{Dt} = \frac{\partial}{\partial t} + (V.\nabla) \tag{3.6}$$

And the τ components represent the normal and shear stresses over the boundaries of the control volume. These are nine new variables in the system; therefore, nine new equations are needed to close the system, each of them can be represented by:

$$\tau_{xy} = \tau_{xy} = \mu\left(\frac{\partial v}{\partial x} + \frac{\partial u}{\partial y}\right) \tag{3.7}$$

$$\tau_{yz} = \tau_{zy} = \mu\left(\frac{\partial w}{\partial y} + \frac{\partial v}{\partial z}\right) \tag{3.8}$$

$$\tau_{zx} = \tau_{xz} = \mu\left(\frac{\partial u}{\partial z} + \frac{\partial w}{\partial x}\right) \tag{3.9}$$

$$\tau_{xx} = \lambda(\nabla.\boldsymbol{V}) + 2\mu\frac{\partial u}{\partial x} \tag{3.10}$$

$$\tau_{yy} = \lambda(\nabla . \boldsymbol{V}) + 2\mu \frac{\partial v}{\partial y} \tag{3.11}$$

$$\tau_{zz} = \lambda(\nabla . \boldsymbol{V}) + 2\mu \frac{\partial w}{\partial z} \tag{3.12}$$

Equations 3.7 to 3.9 represent the shear stresses, while 3.10 to 3.12 are the normal stresses. Where μ is the dynamic viscosity and λ is the bulk viscosity coefficient or second viscosity coefficient. When these equations are combined with equations 3.3 to 3.6 then the full momentum conservation equation or also known as the Navier Stokes equation can be write down.

$$\rho \frac{\partial u}{\partial t} + \rho u \frac{\partial u}{\partial x} + \rho v \frac{\partial u}{\partial y} + \rho w \frac{\partial u}{\partial z} = -\frac{\partial p}{\partial x} + \frac{\partial}{\partial x}\left(\lambda \nabla . \boldsymbol{V} + 2\mu \frac{\partial u}{\partial x}\right) + \frac{\partial}{\partial y}\left[\mu\left(\frac{\partial v}{\partial x} + \frac{\partial u}{\partial y}\right)\right] + \frac{\partial}{\partial z}\left[\mu\left(\frac{\partial u}{\partial z} + \frac{\partial w}{\partial x}\right)\right] \tag{3.13}$$

$$\rho \frac{\partial v}{\partial t} + \rho u \frac{\partial v}{\partial x} + \rho v \frac{\partial v}{\partial y} + \rho w \frac{\partial v}{\partial z} = -\frac{\partial p}{\partial y} + \frac{\partial}{\partial y}\left(\lambda \nabla . \boldsymbol{V} + 2\mu \frac{\partial v}{\partial y}\right) + \frac{\partial}{\partial x}\left[\mu\left(\frac{\partial v}{\partial x} + \frac{\partial u}{\partial y}\right)\right] + \frac{\partial}{\partial z}\left[\mu\left(\frac{\partial w}{\partial y} + \frac{\partial v}{\partial z}\right)\right] \tag{3.14}$$

$$\rho \frac{\partial w}{\partial t} + \rho u \frac{\partial w}{\partial x} + \rho v \frac{\partial w}{\partial y} + \rho w \frac{\partial w}{\partial z} = -\frac{\partial p}{\partial z} + \frac{\partial}{\partial z}\left(\lambda \nabla . \boldsymbol{V} + 2\mu \frac{\partial w}{\partial z}\right) + \frac{\partial}{\partial x}\left[\mu\left(\frac{\partial u}{\partial z} + \frac{\partial w}{\partial x}\right)\right] + \frac{\partial}{\partial y}\left[\mu\left(\frac{\partial w}{\partial y} + \frac{\partial v}{\partial z}\right)\right] \tag{3.15}$$

Now, these equations are complex to solve, with non-linearities and being coupled, therefore, they need to be simplified in order to solve in our case. As an example, we take the x component of the momentum equation and simplify it by assuming that the viscosity is constant as the change in temperature is negligible. We also will assume that our flow is incompressible $\nabla . V = 0$ because the flow speed is in the low subsonic range [15]. When applying the above limitations to the equation of continuity (equation 3.1,) and the equations of momentum (equations 3.13 to 3.15) the result is a simpler and nicer set of equations to deal with:

$$\nabla . \mathbf{V} = 0 \tag{3.16}$$

$$\rho \frac{\partial u}{\partial t} + \rho \left[\frac{\partial}{\partial x}(u^2) + \frac{\partial}{\partial y}(uv) + \frac{\partial}{\partial z}(uw) \right] = -\frac{\partial p}{\partial x} + \mu \left[\frac{\partial^2 u}{\partial x^2} + \frac{\partial^2 u}{\partial y^2} + \frac{\partial^2 u}{\partial z^2} \right] \tag{3.17}$$

$$\rho \frac{\partial v}{\partial t} + \rho \left[\frac{\partial}{\partial x}(uv) + \frac{\partial}{\partial y}(v^2) + \frac{\partial}{\partial z}(vw) \right] = -\frac{\partial p}{\partial y} + \mu \left[\frac{\partial^2 v}{\partial x^2} + \frac{\partial^2 v}{\partial y^2} + \frac{\partial^2 v}{\partial z^2} \right] \tag{3.18}$$

$$\rho \frac{\partial w}{\partial t} + \rho \left[\frac{\partial}{\partial x}(uw) + \frac{\partial}{\partial y}(vw) + \frac{\partial}{\partial z}(w^2) \right] = -\frac{\partial p}{\partial z} + \mu \left[\frac{\partial^2 w}{\partial x^2} + \frac{\partial^2 w}{\partial y^2} + \frac{\partial^2 w}{\partial z^2} \right] \tag{3.19}$$

This is the incompressible version of the continuity and Navier-Stokes equations, as this set of equations remains coupled by their pressure-velocity relation, we will need to select the coupled solver offered by STAR CCM+© in order to solve our cases.

3.4. Reynolds-Averaged Navier-Stokes Equations

Even with a simplified version of the Navier Stokes equation, it is still difficult to come with a solution for most cases, this only gets harder as turbulence gets worse on the system because of the chaotic behavior of fluid particles. One approach to deal with this is to separate the flow variables into two components, a mean or time average component and a fluctuating one [52].

$$\emptyset = \overline{\emptyset} + \emptyset' \tag{3.20}$$

For example, if this is done to the velocity then:

$$\frac{\partial}{\partial x}(u^2) = \frac{\partial}{\partial x}[(\bar{u} + u')^2] = \frac{\partial}{\partial x}(\bar{u}^2 + 2\bar{u}u' + u'^2) \tag{3.21}$$

When applied to the simplified version of the Navier Stokes equations and the time average of the whole expression is considered, then the RANS equations are obtained, here mass conservation and the x component of the momentum equation are shown:

$$\frac{\partial \rho}{\partial t} + \nabla.(\rho \overline{\boldsymbol{V}}) = 0 \tag{3.22}$$

$$\rho \frac{\partial \bar{u}}{\partial t} + \rho \left[\frac{\partial}{\partial x}(\bar{u}^2) + \frac{\partial}{\partial y}(\bar{u}\bar{v}) + \frac{\partial}{\partial z}(\bar{u}\bar{w}) \right] = -\frac{\partial \bar{p}}{\partial x} + \mu \left[\frac{\partial^2 \bar{u}}{\partial x^2} + \frac{\partial^2 \bar{u}}{\partial y^2} + \frac{\partial^2 \bar{u}}{\partial z^2} \right] - \rho \left[\frac{\partial}{\partial x}(\overline{u'^2}) + \frac{\partial}{\partial y}(\overline{u'v'}) + \frac{\partial}{\partial z}(\overline{u'w'}) \right] \tag{3.23}$$

The equations take the same form as the previous instantaneous Navier Stokes equations except that new terms arise now on the right side of the equations, these terms are known as the Reynolds stresses and can be summarized in the Reynolds stress tensor. Now 9 new variables are been introduced to the system, therefore we require new equations to close it, this is known as the turbulence closure problem.

$$\tau_t = -\rho \begin{pmatrix} \overline{u'^2} & \overline{u'v'} & \overline{u'w'} \\ \overline{u'v'} & \overline{v'^2} & \overline{v'w'} \\ \overline{u'w'} & \overline{v'w'} & \overline{w'^2} \end{pmatrix} \tag{3.24}$$

3.5. Introduction to Turbulence models

Several models have been developed to deal with the turbulence closure problem, one approach is to use an eddy viscosity model like the Boussinesq Approximation model [52]. With it, the Reynolds stress components are assumed to be proportional to the mean strain rate tensor S, the eddy viscosity μ_t and the turbulent kinetic energy k_t.

$$\tau_{ij} = 2\mu_t S_{ij}^* - \frac{2}{3}\rho k_t \delta_{ij} \tag{3.25}$$

$$S = \left(\frac{\partial U_i}{\partial x_j} + \frac{\partial U_j}{\partial x_i} \right) \tag{3.26}$$

And δ_{ij} is the Kronecker delta where:

$$\delta_{ij} = 1 \; if \; i = j \;\; and \;\; \delta_{ij} = 0 \; if \; i \neq j \tag{3.27}$$

The premise of this is to relate the momentum flux associated with the molecular motion fluctuations represented by the Reynolds stresses to a molecular viscosity that can be related to the eddies[52]. Although an equation was introduced for each term of the Reynolds stress tensor, two new variables were also introduced, the μ_t and k_t, therefore a way to model them is required. Several approaches have been studied and different models have surged varying between their complexity, accuracy and computational cost to deal with the problem. Their range varies from simple only one additional equation required find in models like Spalart Allmaras, to two additional equations like k-ϵ, k-ω and k- ω Shear Stress Transport (SST), to more complete models like the Reynolds Stress equation model where, it is attempted to solve directly for the Reynolds stresses without using the Boussinesq approximation by introducing 6 new equations. For our work, the k-ω SST model was chosen and therefore it will be explained in the subsequent chapter along with its relationship with the k-epsilon and standard k-omega models.

3.6. The k- ω model

The k- ω model solves for the turbulent eddy viscosity by introducing a new variable known as the specific dissipation rate ω which is proportional to the turbulent dissipation rate ϵ per unit of turbulent kinetic energy k. [45]. These variables are related to the Boussinesq approximation by assuming the turbulent eddy viscosity to be equal to:

$$\mu_t = \rho k T_{ts} = \rho k \frac{\alpha^*}{\omega} \tag{3.28}$$

Where T_{ts} is the turbulent time scale and for the standard k-ω model is equal to α^* which is a modal coefficient over ω. Then, each variable (k and ω) are solved by using their respective transport equations:

$$\frac{\partial}{\partial t}(pk) + \nabla.(pk\bar{V}) = \nabla.[(\mu + \sigma_k\mu_t)\nabla \mathrm{k}] + \mathrm{P_k} - \rho\beta^* f_{\beta^*}(\omega k - \omega_0 k_0) + S_k \tag{3.29}$$

$$\frac{\partial}{\partial t}(p\omega) + \nabla.(p\omega\bar{V}) = \nabla.[(\mu + \sigma_\omega\mu_t)\nabla\omega] + \mathrm{P}_\omega - \rho\beta f_\beta(\omega^2 - \omega_0^2) + S_\omega \tag{3.30}$$

Where $\bar{V}$ is the mean velocity, σ_k and σ_ω are model coefficients, P_k and P_ω are production terms, f_{beta^*} is the free shear modification factor, f_{beta} is the vortex stretching modification factor, S_k and $S_\omega$are user-defined source terms and k_0 and ω_0 are the ambient turbulence values. The production terms are defined as:

$$P_k = G_k + G_{nl} + G_b \tag{3.31}$$

$$P_k = G_\omega + D_\omega \tag{3.32}$$

Where G_k is the turbulent production term, G_{nl} is the nonlinear production, G_b is the buoyancy production, G_ω is the specific dissipation production and D_ω is the cross-diffusion term.

It could be argued that one of the reasons for the creation of the k-ω model was that the k-ϵ model was having trouble with boundary layers when an adverse gradient in pressure is present, while the k- ω has proven to be better to resolve the flow over this region [55]. Although as a counterpoint the k- ω model experiences difficulties involving sensitivity between the boundary layer and the ω value in the free stream flow [45]. That been said, Menter [56] came with a solution by combining both models and by so obtaining the benefits of the k-ϵ model over

the free stream flow with the resolution near the wall done by the k-ω model, this is known as the Menter's SST k-ω model.

The approach suggested by Menter was to change the k-ϵ transport equation by applying variable substitution into the k-ω transport equation [56]. These equations would have similar form and yield similar results except for a non-conservative cross-diffusion term pointed out on equation 3.34. As such, Menter suggested to use a blending function dependent on the wall distance that would account for the said term when solving inside the far-field region (where k-ϵ is best) and to disregard it when closer to the wall (where standard k-ω is favored). By doing so the cross-diffusion term takes the form of

$$D_\omega = 2\rho(1 - F_1)\sigma_{\omega_2}\frac{1}{\omega}\nabla k.\nabla\omega \tag{3.33}$$

Where F_1 is a blending function equal to:

$$F_1 = \tanh\left(\left[min\left(max\left(\frac{\sqrt{k}}{0.09\omega d}, \frac{500v}{d^2\omega}\right), \frac{2k}{d^2 CD_{k\omega}}\right)\right]^4\right) \tag{3.34}$$

Where d is the distance to the wall and $CD_{k\omega}$ is a cross-diffusion coefficient. Because of this, Menter also changed and introduced a blending function when calculating for the turbulent time scale as:

$$T = \min\left(\frac{\alpha^*}{\omega}, \frac{a_1}{SF_2}\right) \tag{3.35}$$

Where α^* and a_1 are model coefficients, S is the modulus of the mean strain rate tensor and F_2 is a blending function calculated as:

$$F_2 = \tanh\left(\left(max\left(\frac{2\sqrt{k}}{\beta^*\omega d}, \frac{500v}{d^2\omega}\right)\right)^2\right) \tag{3.36}$$

Where β^* is a model coefficient and d is the distance to the wall. All model coefficients values and/or ways to calculate them can be found inside the STAR CCM+© theory manual [45]

3.7. Force calculation

In order to analyze and compare VAWTs we can rely on common aerodynamic variables such as lift, drag and moment as experienced by the airfoil, and then estimate the power output produced by the turbine. In Star CCM+ we can track the forces acting on the airfoil's surface by creating a "force report", this type of report can sum the forces acting on a surface if we indicate the direction to where the forces should be computed.

$$f = \sum_f \left(f_f^{pressure} + f_f^{shear}\right).n_f \tag{3.37}$$

Where $f^{pressure}$ and f^{shear} are the pressure and shear force vectors over the surfaces respectively, and n_f is the user-specified direction vector. The pressure and shear forces are calculated as:

$$f_f^{pressure} = \left(p_f - p_{ref}\right)\boldsymbol{a}_f \tag{3.38}$$

$$f_f^{shear} = -\boldsymbol{T}_f.\boldsymbol{a}_f \tag{3.39}$$

Where p_f is the face static pressure, $\boldsymbol{a}_f$ is the face area vector, p_{ref} is the reference pressure and T_f is the stress tensor over the surface. To calculate lift and drag it is necessary to separate the pressure and shear forces in components that are tangential and normal to the airfoil. This is done first by choosing two-directional unitary vectors n_f, according to a Cartesian coordinate system,

and then multiplying them to the pressure and shear forces to get the x and y force components F_x and F_y. Because of the airfoil being in constant rotation, the x and y force components cannot represent accurately the normal and tangential forces, therefore, to account for the rotation a modified equation it is used that considers the azimuthal position of the airfoil.

$$F_N = F_y \cos\theta - F_x \sin\theta \tag{3.40}$$

$$F_T = F_y \sin\theta + F_x \cos\theta \tag{3.41}$$

Where θ is the azimuthal angle of the airfoil. Then to get the lift and drag:

$$L = F_N \cos(\alpha + i) - F_T \sin(\alpha + i) \tag{3.42}$$

$$D = F_N \sin(\alpha + i) + F_T \cos(\alpha + i) \tag{3.43}$$

Where i is the incidence angle dependent on the airfoil's camber and α is the angle of attack between the relative velocity and the airfoil's chord. The angle of attack is dependent on the azimuthal position and the tip speed ratio of the blade.

$$\alpha = \arctan\left(\frac{sin\,\theta}{cos\,\theta + TSR}\right) \tag{3.44}$$

Even though we are able to calculate the lift and drag, in order to compare them to other wind turbines it is good practice to normalize the variables by writing them down as lift and drag coefficients.

$$C_L = \frac{L}{0.5\rho_\infty V_{rel}^2 c} \tag{3.45}$$

$$C_D = \frac{D}{0.5\rho_\infty V_{rel}^2 c} \tag{3.46}$$

Where ρ_∞ is the free stream density, and c is the blade's chord length. The other important coefficient that it is needed to calculate is the power coefficient which is dependent on the torque experienced by the airfoil, this can be done by creating a "moment report" over the airfoil's surface, it will consider the tangential force times the radial distance. After this, the power output will be equal to the torque times the angular velocity.

$$Tor = F_T r \tag{3.47}$$

$$P = Tor\omega \tag{3.48}$$

Finally, the power coefficient can be calculated as:

$$C_P = \frac{P}{0.5\rho_\infty V_{rel}^3 A} = \frac{Tor\omega}{0.5\rho_\infty V_{rel}^3 A} \tag{3.49}$$

3.8. Boundary layer model

One of the most important features to capture when creating a new aerodynamic simulation is the boundary layer which is a small film/layer that forms due to the viscous effects of a fluid and its interaction with an object's surfaces when it's moving relative to it. Aerodynamic forces like lift and drag depend on the boundary layer and how it develops over the surface, this depends on flow properties like the flow's velocity, density, viscosity and the object's shape too [57].

The boundary layer can be subdivided into three different layers depending on the viscous and inertial effects within them. The first one which is in contact with the wall is the

viscous sublayer, where viscous effects dominate and the flow characteristics are almost laminar. Next to it is the buffer layer which stands as a transitional layer between the viscous sublayer and the third one, the log-law layer, inside the latter the flow characteristics are equally dominated by the viscous and the turbulent (inertial) effects [57] It is important to differentiate them in order to model them correctly, by convention this is usually done by using the y+ value, a non-dimensional distance to the wall calculated as:

$$y^+ = \frac{yu^*}{\nu} \tag{3.50}$$

$$u^+ = \frac{u}{u^*} \tag{3.51}$$

$$u^* = \sqrt{\frac{\tau_w}{\rho}} \tag{3.52}$$

Where y is the normal distance from the wall-cell centroid, u* is a reference velocity, ν is the kinematic viscosity, u is the component of the velocity parallel to the wall, ρ is the density and $\tau_w$is the wall shear stress. Figure 18 shows the non-dimensional velocity u+ been plotted against the y+ and shows the behaviors associated with the three sublayers.

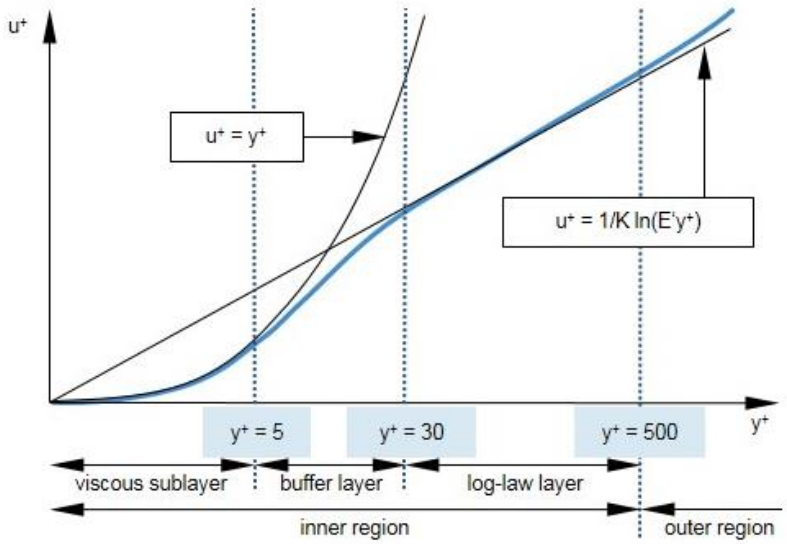

Figure 18- Non dimensional velocity u+ vs y+ showing the three sublayers and their associated tendency functions [45]

Once the layers have been identified, one needs to choose what is it call inside Star CCM+ as a wall treatment. Depending on the y+ value the software will try to model or, if possible, to solve for the flow inside the layers. For our case, it was chosen the "all-y+ wall treatment" which is a hybrid scheme between the low and high wall treatment approaches inside Star CCM+, those two are designed to work for fine and coarse meshes respectably. The reason behind this was due to the use of a dynamic mesh that will constantly rotate and eventually morph to a new shape for the blades, this inevitably changes the y+ value during the whole simulation. If some wall-cells are outside of the viscous sublayer by an increased y+ value later in the simulation, then all-y+ wall treatment can account for this by using a blending function when these cells enter the buffer layer. If the y+ value is maintained below the buffer layer threshold, then the wall treatment would be equal to the low value one. Figure 19 exemplifies the use of the all-y wall treatment.

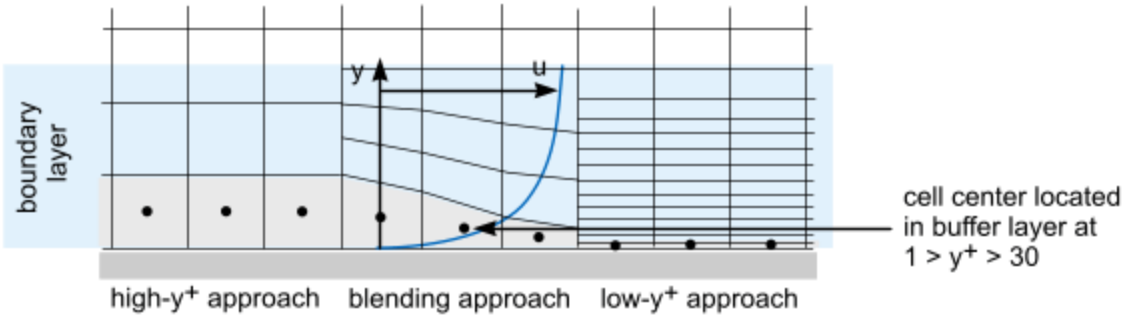

Figure 19- Diagram showing the concept of the All y+ wall treatment used inside Star CCM+ [45].

3.9. Dynamic Mesh

In chapter 2 a brief introduction to the dynamic mesh theory was given, here we will expand on how STAR CCM+ implements these methods, particularly for overset meshes and morphing capabilities. Ultimately the reason behind choosing to overset meshes instead of sliding ones stands on the possibility of using overset meshes plus the morphing mesh at the same time, something not possible inside STAR CCM+ when the sliding mesh was selected. Although the computational cost is higher for the overset mesh to simulate the rotational movement, the relatively small size of the mesh and its boundary does not make it expensive enough to pursue other methods.

3.9.1. Overset mesh

The key feature of this method is to split the mesh domain into separate regions, one background and the other overset, where we can move the latter independently from the first one and recreate an arbitrary movement like the rotation in a VAWT. The relation between the background and overset mesh will be explain using Figure 20 which is extracted from the STAR CCM+ user manual [45], this will help us explain how the communication between both meshes works.

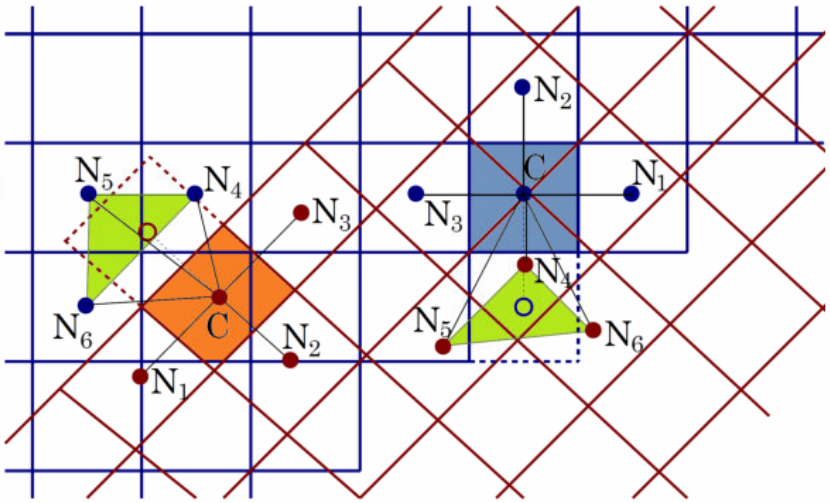

Figure 20- Representation of the donor-acceptor relation at the boundary for overset meshes. [45]

The idea revolves around active and inactive cells, acceptors and donors. The inactive cells are those that were cut out from the background mesh, while the rest will be the active ones. Then a "layered approach" is used, this is constructing a layer of acceptor and donor cells around the interface containing the overset region. These cells oversee the communication, an acceptor cell will need at least one donor to function, and depending on the interpolation (distance-weighed, linear or least squares) could be more. According to Mclean [53] which studied VAWT using overset meshes, the linear interpolation provided the most accurate results for the rotation.

In the figure shown, when we try to calculate a variable's value on a cell "C" and we are using linear interpolation, we need 6 other cells to do it. N1-3 represents the cell's variable value for the neighbor cell on the same mesh, while N4-6 are the values on the donor cells for the other mesh, forming the interpolation element (the green triangle). These N4-6 values are used to calculate a new value for the acceptor cell (demarked by the dotted line and an "O" for its centroid), this is done using:

$$\phi_{acceptor} = \sum \alpha_i \phi_i \tag{3.53}$$

Where $\phi_{acceptor}$ is the variable of interest on the acceptor cell, α_i are the interpolation weighing factors, and ϕ_i are the values of the dependent variables at the donor cells [45]. By doing this, the fluxes between the cell "C" and the acceptor can be calculated, and the connection between both meshes is established.

One issue related to the use of the interpolation technique in the boundary between the background and overset meshes is that it is not a conservative scheme, and therefore a mass imbalance appears over this region. To counter this weakness, STAR CCM+ has two techniques available, a source term correction and a flux correction. The former uses the segregated solver and adds a mass source to the discretized pressure-correction equation to cancel the imbalance created by the interpolation. The latter adjusts the sum of the interface fluxes to be equal to zero by subtracting a part of the mass source $\Delta\dot{m}$ (created by the mass imbalance) to each mass flux $\dot{m}$ [45].

$$\dot{m}^{corr} = \dot{m}_i - \beta_i \Delta\dot{m} \tag{3.54}$$

Where β_i is a proportionality factor.

3.9.2. Morphing mesh

In the case of the morphing method, the initial movement is set by STAR CCM+ using a series of control vertices, each of them associated with a displacement vector in order to move neighbor vertices. These displacements are defined by interpolation fields created with Radial Basis Functions (RBF) inside STAR CCM+, each displacement "d_i" can be defined for each vertex as:

$$d_i = \sum_{j=1}^{N} f_{b,j}(r_{ij})\boldsymbol{\lambda_j} + \boldsymbol{\alpha} \tag{3.55}$$

Where f_{bj} is a radial basis function of the form:

$$f_{b,j}(r_{ij}) = \sqrt{r_{ij}^2 + c_j^2} \tag{3.56}$$

And r_{ij} is the magnitude of the distance between two vertices.

$$r_{ij} = |\boldsymbol{x}_i - \boldsymbol{x}_j| \tag{3.57}$$

Here λ represents an expansion coefficient, x_i is the position of the vertex, N is the number of vertices, C_j is the basis constant, and α is a constant vector. And the additional equation is needed to account for an additional constraint where the sum of all expansion coefficient should be equal to zero, this is done to bound the movement of vertices located far away.

$$\sum_{j=1}^{N} \lambda_j = 0 \tag{3.58}$$

When a user-specified displacement is used to deform an airfoil's shape, it is necessary to avoid big "jumps" between frames of motion. This means the motion needs to be smoothed between the initial and final shape for the airfoil if not, the sudden change will create large imbalances in the conservation equations and make the solution unstable. To address this and improve smoothness, a damping function is applied, which is dependent on the vertices' distance to the airfoil's walls.

4. Validation case

There are certain types of tests that can be done in order to choose proper conditions for our simulations, a sensitivity test applied for the grid and time steps used are examples of them, as well as to test the order of temporal discretization scheme to be used. Besides these tests, in order to test the quality of our deforming approach when applied to a VAWT, a baseline scenario is needed to be created and compared to a known case backed up by experimental data. This way the accuracy of the numerical schemes, meshes generated, and physical conditions are validated and we can continue to more complex systems.

4.1. Grid sensitivity analysis

Therefore, consider a simple one blade simulation of a VAWT in 2D as the base scenario, with it we will compare the power coefficients between different levels of grid refinement by changing the number of cells inside the domain while maintaining the same geometry and boundary conditions. When the difference between the grids' results is sufficiently small, the solution is said to be relatively independent of the mesh size.

Besides the grid's spacing, one must account for the case's time step sensitivity, this is, how much the answer depends on the size of the time step chosen, this dependency arises from how the conservation equations are discretized, whereas an explicit or implicit method is chosen, and on the order of the discretization scheme used [58]. Because our VAWT model also deals with the deformation of its airfoils besides the normal rotational motion, the time step also controls how fast the airfoil deforms. A bigger time step means a bigger "jump" between frames of movement while the angular velocity stays the same, our experience has shown that this could cause instabilities in the solution, which may be due to the sudden change in local variables

between the old and new position. Because of this, the time steps should remain sufficiently small in order to let a smooth transition but not so much as to make the simulation too expensive as it will take longer to compute each cycle. As suggested by Tan [44] and McLean [53], dividing each cycle into 2000 and 3000 steps serve as good indicators to test the time step size, as they give each frame 0.18 and 0.12 degrees of motion per time step, which for a 90 RPM angular velocity corresponds to time steps equal to 3.333E-4 s and 2.222E-4 s respectively.

Four meshes were generated with resolutions marked as "courser", "intermediate", "finer" and "finest", as an example, a series of figures showing the results of the finer mesh is presented over Figures 21-24. These meshes were tested using the same boundary and initial conditions, only differing on their level of refinement by their cell number count, the geometrical, mesh and initial conditions are shown in Table 1.

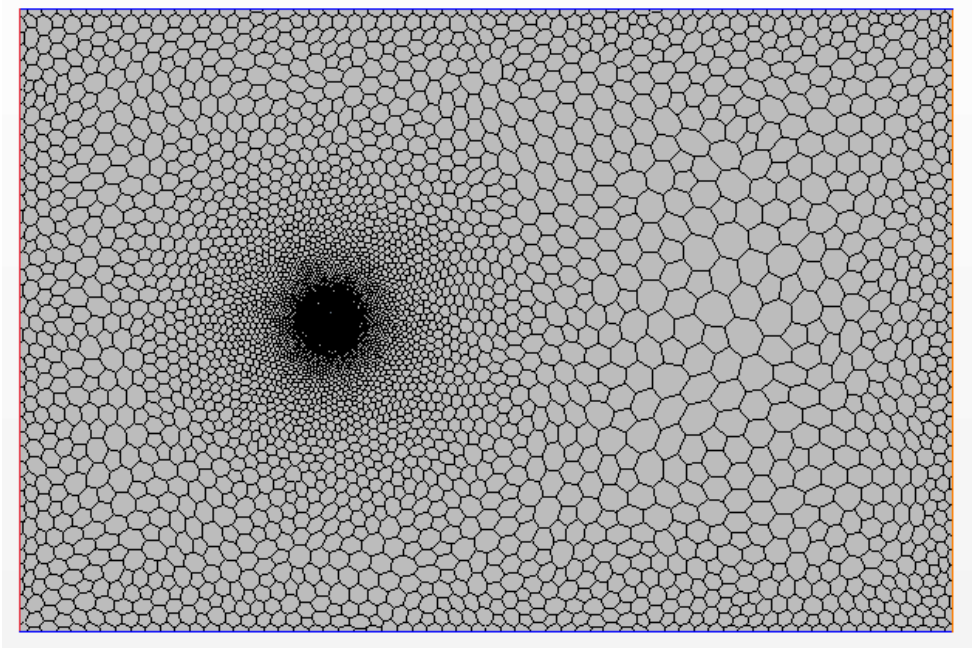

Figure 21- Whole mesh domain, mostly composed by a course background mesh except near the airfoil where a heavily dense mesh is set.

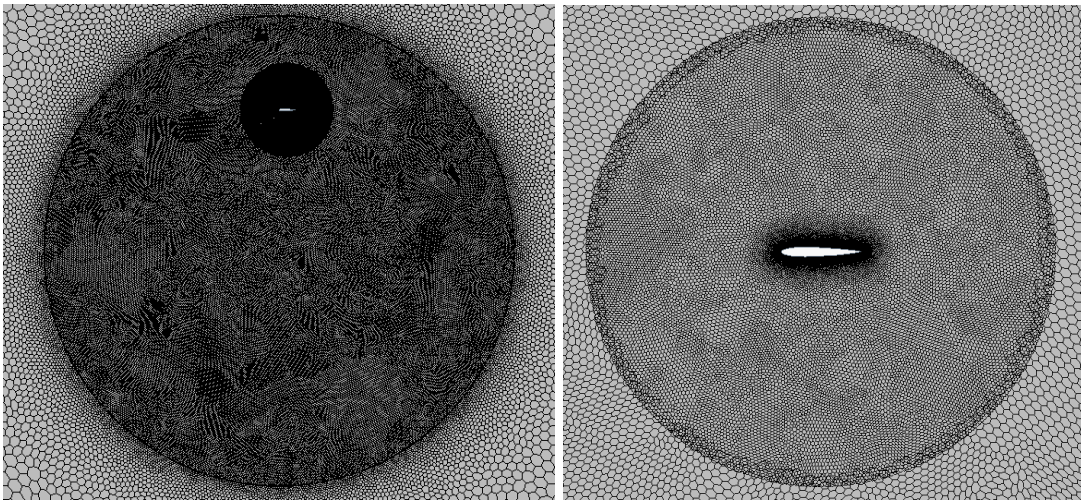

Figure 22- Refined background mesh region (left). Overset mesh region after initialization, the background/overset mesh boundary can be seen. (right)

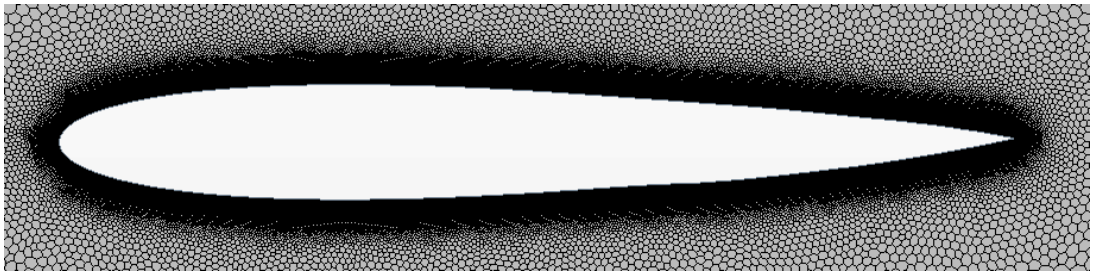

Figure 23- View of overset mesh around the airfoil.

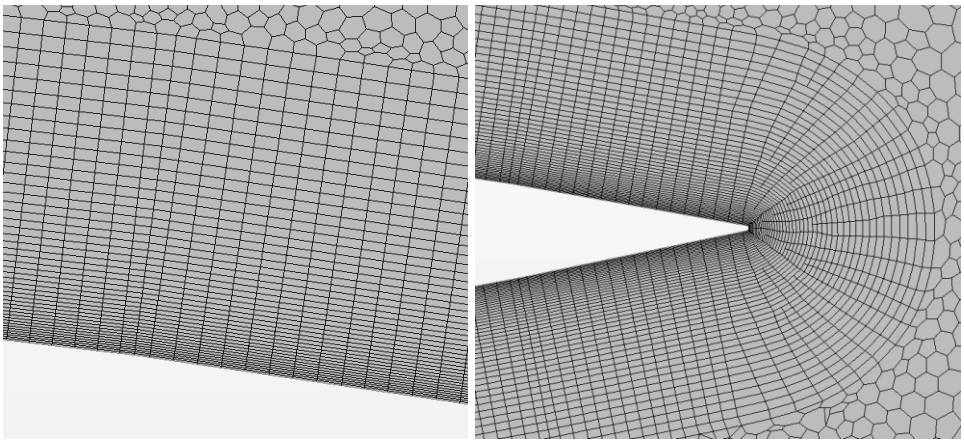

Figure 24- Prism mesh layers over the airfoil's surface.

Table 1 - Summary of geometrical, mesh-related and initial conditions.

Parameter	Value
Number of blades	1
Rotor diameter	5.395 m
Airfoil chord length	0.303 m
Rotor angular velocity	90 RPM
Turbulent intensity	0.05 %
Turbulent viscosity ratio	0.1
Inlet velocity	8 m/s
Tip Speed Ratio	3.17
Number of prism layer	80
Prism layer near-wall thickness	1.0E-5 m
Prism layer total thickness	0.02 m
Number of nodes on the airfoil	1957
Static temperature	293.15 K

Before running the cases to validate the methodology, it is needed that the numerical schemes are set up properly, this is done by choosing the more suitable discretization schemes for our case. Some are chosen based on previous experience, while others are tested to examine its behavior like the temporal discretization order. As a rule, all numerical schemes selected for simulations inside this section are specified in Table 2 unless mention otherwise.

Table 2- Numerical schemes applied to simulations in section 4.

Temporal solver	Implicit unsteady
Temporal discretization	Second Order
Flow solver	Coupled flow- Implicit
Spatial discretization	Second Order Upwind
Turbulence model	Menter's SST K-Omega
Equation of state	Ideal Gas
Wall treatment	Low y+

To estimate the power output for a VAWT and understand its vortex shedding behavior it is necessary to run an unsteady case where we can observe the solution as it changes over time, to do this it is important to select an appropriate temporal solver. An implicit type of solver was chosen because even though the time step is quite small and it could favor explicit schemes (as they are quicker to solve per iteration), the more stable nature of an implicit solver is preferable considering the complex flow's behavior [58]. It also must be mention that because of the implicit scheme, it is not necessary to strictly satisfy the Courant-Friedrichs-Lewy condition like for explicit schemes, where the CFL number needs to be below 1 for the solution to be stable [58]. This allows the time step to be much bigger while maintaining stability, which in turn decreases the processing time of each cycle greatly.

Flow and energy solvers were chosen to be coupled schemes as suggested by McLean [53] because segregated schemes gave convergence issues for the mass continuity and momentum residuals. This could be related to that coupled schemes tend to be more robust when dealing with flows with strong source terms such as rotation when compared to segregated ones [45].

STAR CCM+ only allows to choose between first and second-order upwind and MUSCL third order/CD schemes for this case, like other types of schemes like central/bounded-central or hybrid/hybrid-BCD, are offered only to use with Large Eddy Simulations (LES) or Detached Eddy Simulations respectively [45]. Between the first and second-order upwind schemes, it is preferred to use the latter mainly because of its higher accuracy, even though it is less stable than the former [58]. It must be mentioned that Pletcher *et al.* [59] has found problems with numerical diffusion when using the first-order upwind scheme. On the other hand, Tan [44] suggested that using the higher-order MUSCL scheme to simulate a similar 2D VAWT case could be too unstable, therefore as a tradeoff, it was chosen to use a second-order upwind scheme for the

spatial discretization. After running the cases, the results were compared using their power coefficients and grid refinement levels for each time step, their results are presented in Figures 25 and 26.

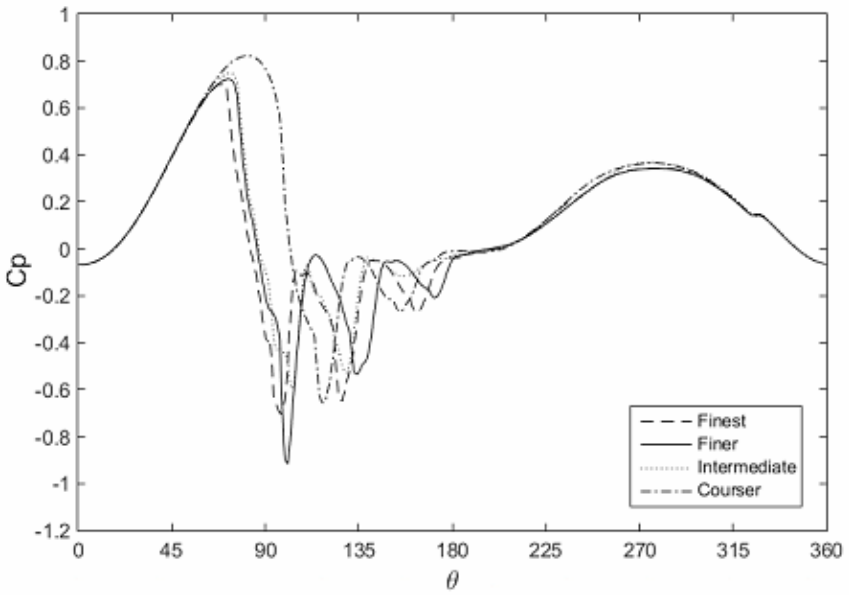

Figure 25- Power coefficient comparison between grid refinements for the time step 3.333E-4 s.

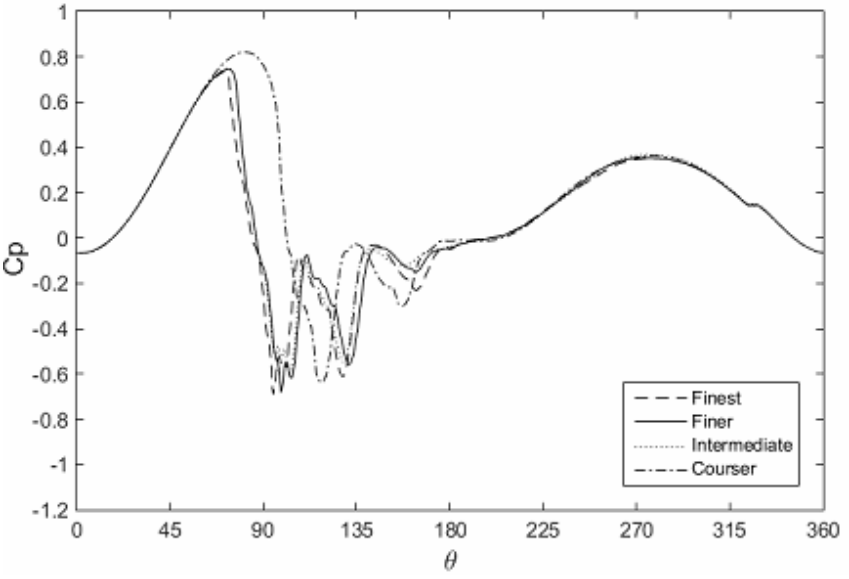

Figure 26- Power coefficient comparison between grid refinements for the time step 2.222E-4 s.

By examining the power coefficient plots, the main difference between them is between the 90-180 degrees region where the vortex shedding is expected to appear. As the mesh is refined the vortexes are better captured, therefore revealing a stronger recirculation region over the airfoil that by detaching will decreasing the total power outlet. Table 3 summarizes the averaged power coefficients obtained, as expected for this case a courser mesh will give a higher averaged power coefficient as the negative region will decrease in size by not being captured properly, therefore giving a false sense of better performance.

There is a limit by how much we can refine the mesh due to computational costs, as such we argue that to use the 3rd or the "finer" mesh model is best suited for our necessities instead of the finest one. This is due to the difference in the averaged value for power coefficient becomes as small as 5,3 % between the intermediate and finer meshes for the smaller time step, which is considered to be small enough at this point (bearing in mind that we are dealing with a complex flow in an unsteady solution). It is worth point out that even though the solution doesn't seem to show an absolute convergence over the whole cycle, for most of it the solutions seem to overlap between different mesh sizes, the biggest issue as excepted is localized over the second quadrant where dynamic stall appears. Here dispersion between the curves is visible, although the smaller time step seems to better capture the vortexes as seen in Figure 26, where the curves seem to overlap better, being less disperse.

It is also considered that the "finest" mesh only offers a small gain in the results at the expense of a much heavier mesh to run (when compared to the previous cases), as such this extra computational cost is preferred to be avoided. Regarding the time step size, when a smaller value is used the change in the averaged power coefficient between meshes becomes smaller, this and the fact that a smaller time step will improve stability (especially when deforming capabilities are

applied as explained before) make it easy to choose the time step to be equal to 2.222E-4 s. As such, for the baseline case, it is decided that the best option is to use the "finer" mesh with a time step equal to 2.222E-4 s.

Table 3- Mesh cell number and averaged Cp obtained from the sensitivity analysis.

Grid	Cell number	Average Cp (3.333E-4 s)	Average Cp (2.222E-4 s)
Courser	185323	0.15588	0.15063
Intermediate	318619	0.10680	0.10157
Finer	416462	0.08968	0.09608
Finest	561619	0.07937	0.08722

It should be mention that the resolution of the boundary layer surrounding the airfoil was also considered, this region is of vital importance for the study of VAWT as it relates directly to the dynamic stall and vortex shedding previously discussed in chapter 3. In our study, the y+ distribution along the blade was maintained for all the cases and its values are shown in the next figure. Because of the continuous rotation of a VAWT, the y+ oscillates constantly due to changes in the relative velocity as seen by the blade, therefore we need to consider the worst-case scenario where this velocity is greatest. For our case, this happens near the region where the azimuth position is close to 0 degrees as seen in Figure 8, therefore y+ values were captured here and are shown in Figure 29. Most elements have a y+ lower than 1, which is more than appropriate to avoid the buffer layer and thus allow the use of the SST k-ω turbulence model.

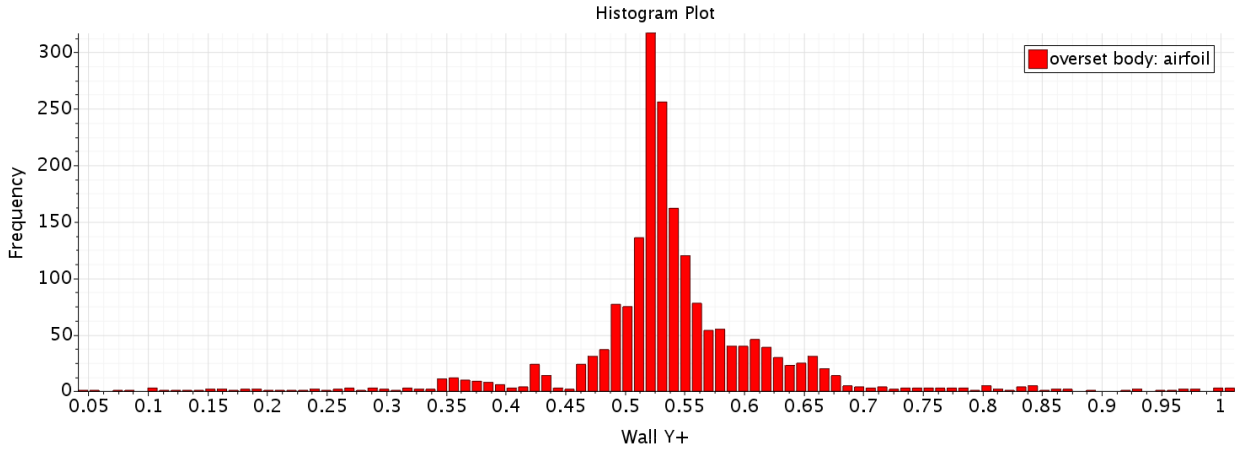

Figure 27- Histogram plot showing wall y+ value vs frequency for the finer mesh.

4.2. Comparison with experimental results

After the grid and time step sensitivity tests are done, we can have a certain degree of confidence in our results, but this doesn't mean that the equations represent accurately the actual physics. The tests only oversee that changes in the grid and time step won't change the values of interest. To validate our methodology, we need to build a case to be used as a baseline and compare it against other CFD and/or experimental results found in the literature.

For comparison, we choose the test case done by Castelein [60] which was designed to be used as a benchmark scenario for numerical validations of VAWT cases. The case consists of 2 rotating blades using NACA0018 airfoils, a blade span of 1 m, a blade chord length of 0.06 m and a rotor radius of 0.5 m. The turbine operates at TSR = 2 with a free stream velocity of 10.2 m/s. Particle Image Velocimetry (PIV) was chosen by Castelein [60] as a measurement technique, the measurements were taken at the blades' midspan in order to minimize the influence caused by the tips of the blades on the flow. This provides an opportunity to study 2D cases in CFD, and to compare them against the results obtained from Castelein to validate the methodology used.

To generate the mesh for the baseline, STAR CCM+ allow us to choose between tetrahedral, hexahedral and polyhedral cells, any of them can be converted to 2D during the mesh processing by choosing one of the symmetric boundary faces and applying a "badge for 2D meshing" which allows to only use that face for the simulation [45].

In our case we argue that Polyhedral/polygonal meshes are more advantageous than tetrahedral ones because the latter could be merged to form polyhedral cells, this action reduces the total number of cells, therefore reducing the computational cost. It also could improve the overall mesh quality by reducing the skewness of the cells by combining badly skewed neighboring cells. Another argument in favor of polyhedral meshes is that by having a higher number of neighbor cells (an average of 14 cell faces [45] against 4 in tetrahedral) the gradients and local flow distributions can be better approximated than by using tetrahedral/hexahedral.

STAR CCM+ guidelines also recommend the use of polyhedral meshes for flows that tend to change directions abruptly, arguably although not mentioned directly on the manual because of how polyhedral cells are(usually) not align with the flow (when looking at their relative centroid positions). This makes the mesh to be less dependent on the flow's direction, which is beneficial to our case where part of the domain itself will be rotating. Although as a counterpoint it must be mention that as polyhedral meshes are less likely to be aligned with the flow, problems with velocity and pressure calculations could arise as accuracy goes down per cell. Considering the reasons mentioned above, it was decided that the use of polyhedral meshes have satisfied the need for the present study.

A summary of the geometrical and mesh parameters, as well as initial conditions for the present case, can be found in Table 5, while information related to the numerical setup can be

found in Table 6. The mesh itself is presented in Figures 30-33 where three regions are distinguished, first, there is the outer domain that although encompass most of the computational domain's space, it has the smallest number of cells in it as it is far away from the blades. Then it is the rotor's region where a surface control was applied and the cells were refined to better capture flow's features after it interacts with the blades and sheds downstream. Finally, there is the near airfoil region, where the higher density of cells is placed to properly capture the boundary layer (with prism cells). It is worth to point out that we are already using overset meshing techniques to simulate the VAWT's movement on this simulation. Even though a sliding technique approach would be arguably cheaper to run as the interpolation is less complex than the one related to the overset method, the latter allows us to employ both rotation and deformation/morphing techniques over the mesh which is central to this study.

Table 4-Summary of geometrical, mesh-related and initial conditions for the experimental case comparison.

Parameter	Value
Number of blades	2
Rotor diameter	1 m
Airfoil chord length	0.06 m
Rotor angular velocity	389.6 RPM
Turbulent intensity	0.05 %
Turbulent viscosity ratio	0.1
Inlet velocity	10.2 m/s
Tip Speed Ratio	2
Number of prism layer	80
Prism layer near-wall thickness	1.0E-5 m
Prism layer total thickness	0.004 m
Number of nodes on the airfoil	1054
Static temperature	293.15 K

Table 5-Numerical setup applied to for the experimental case comparison.

Temporal solver	Implicit unsteady
Temporal discretization	Second Order
Flow solver	Coupled flow- Implicit
Spatial discretization	Second Order Upwind
Turbulence model	Menter's SST K-Omega
Equation of state	Ideal Gas
Wall treatment	Low y+

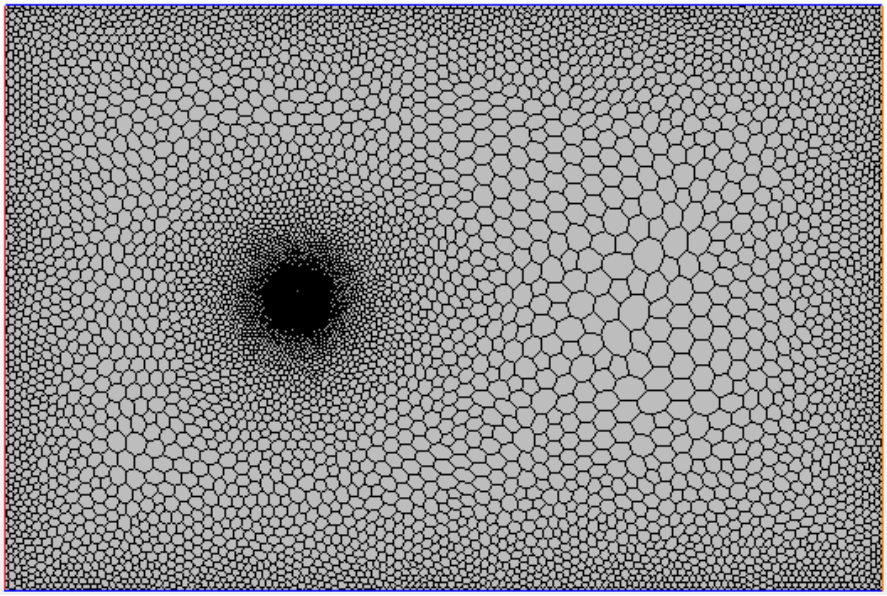

Figure 28-Whole mesh domain for the experimental case comparison.

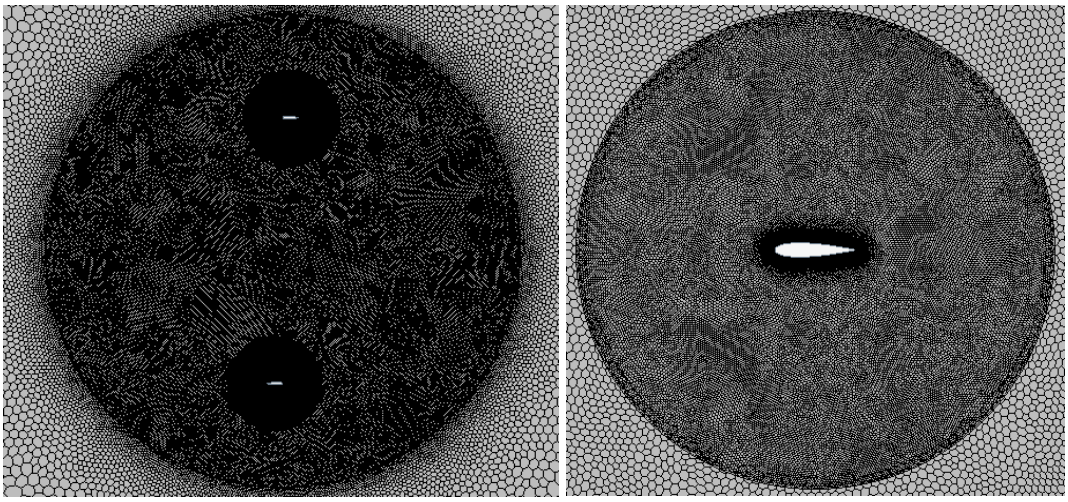

Figure 29-For the experimental case. Refined background mesh region (left). Overset mesh region after initialization. (right)

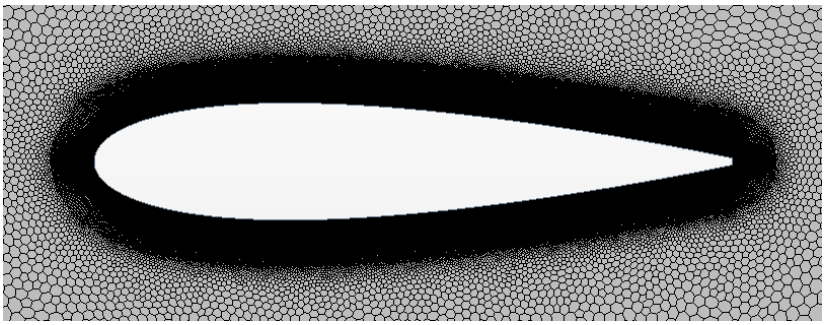

Figure 30-View of overset mesh around the airfoil for the experimental case.

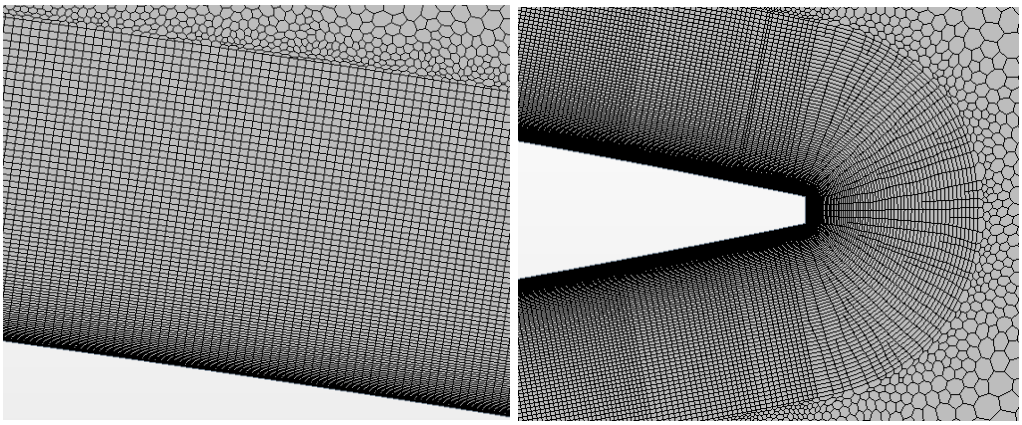

Figure 31- Prism mesh layers over the airfoil's surface. for the experimental case.

Although useful, polygonal elements shouldn't be applied over all the computational domains, for example, there is an important region over the airfoil where the boundary layer forms and needs to be captured. Polygonal elements could be used in this region but at the expense of the mesh needing to be too fine. Instead STAR CCM+ offers the possibility to apply prism layers to wrap around the object in question, this allows to capture more efficiently the boundary layer once the elements can be densely packed near the airfoil's surface by placing them in an orderly fashion (been almost perpendicular to the wall) and allowing a high aspect ratio in the stream direction. However, when prism layers were used it was observed that the cells tend to "collapse" near the trailing edge, this means that the prism layers tend to disappear until the point there is no more and only leaves polyhedral cells being attached to the wall at the trailing edge. According to the STAR CCM+© manual [45], this is likely caused by sharp corners in the geometry where is challenging to locate quality perpendicular prism layers around the corner. To fix this issue the option "advance layer mesher" was used, this feature helps the user to force certain conditions on the mesh near the walls, like maintaining the prism layer thickness, which enables us to cover the entire airfoil without the previous total collapse of cells near the trailing edge.

Finally, Figures 34 and 35 show a comparison between the non-dimensionalized normal and tangential forces between our verification case and the benchmark test case from Castelein [60]. As it can be seen from both figures, there is a good agreement between the results for the most part of the cycle, however on the first half there is some mismatch, this is most likely due to to the vortex shedding that is expected to happen in the vicinity of this region. Figure 36 helps visualize the complexity of the flow by showing a snapshot of the vorticity. It can be seen the

interaction between the flow and the blades as the wake encounters them on the second half of the cycle

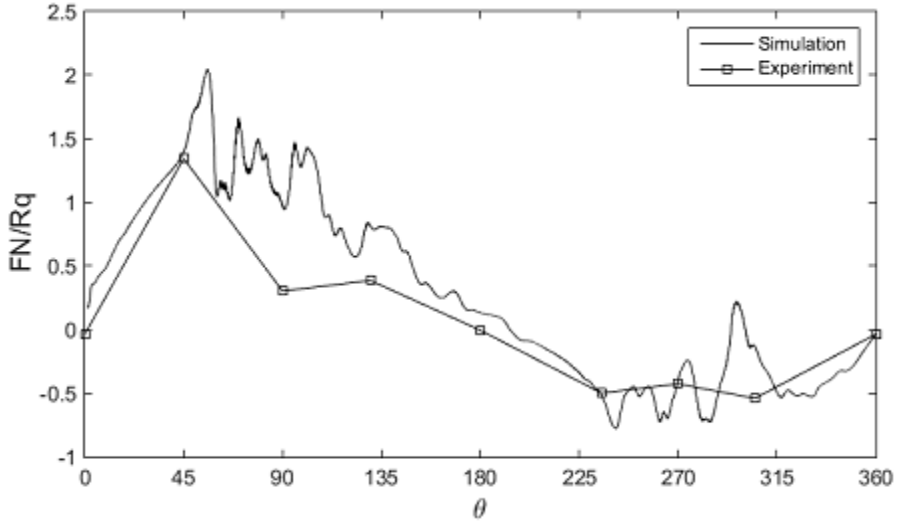

Figure 32- Non-dimensionalized normal force vs azimuthal angle comparison between Castelein's experimental results and our CFD verification case for a TSR=2. [60]

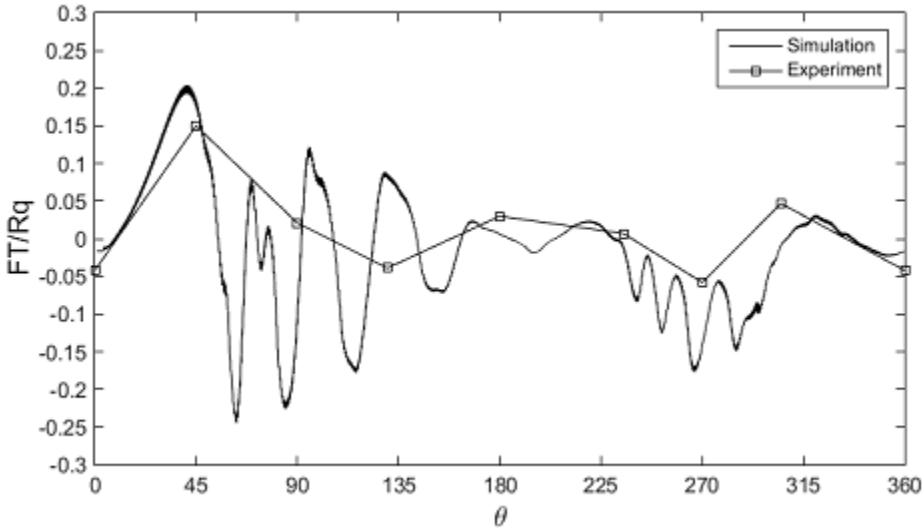

Figure 33-Non-dimensionalized tangential force vs azimuthal angle comparison between Castelein's experimental results and our CFD verification case for a TSR=2. [60]

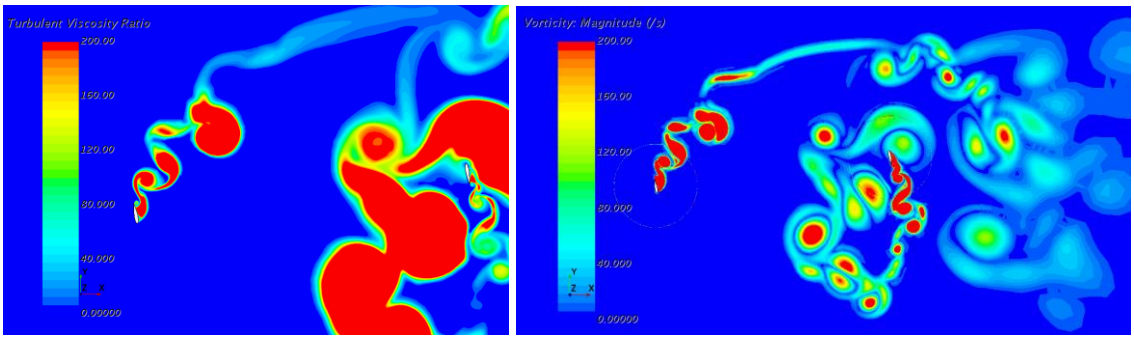

Figure 34-Comparison between turbulent viscosity ratio and vorticity magnitude for the validation case to compare with Castelein's experiment [60].

5. Results and Discussion

This chapter is dedicated to studying the performance of a deforming airfoil scheme applied to a VAWT, this is done by running a baseline and a deforming case while comparing their power coefficients, as well as regarding other features like; aerodynamics forces over the airfoil, pressure and vorticity nearby and downstream from the blade, and studying the changes in the mesh quality as the airfoil deforms. This study differentiates from others as it allows the study of a rotating and deforming airfoil at the same time, something usually not possible as it is common to test an airfoil's shape, gather data, and then retest the case with a new airfoil's geometry. When all the shapes are tested a final plot can me mounted signalizing the areas where the new shapes performed best, although useful, this practice doesn't account for the (although small) transition time between frames that could influence the flow. This simultaneous rotating-deforming approach also allows studying the vortex shedding phenomenon and its possible mitigation/control by the deforming technique.

5.1. Fixed shape rotating airfoil – Baseline case

In chapter 4 a validation study was done and the mesh characteristics, as well as numeric parameters, were discussed and chosen. For the baseline case, the "finer" mesh will be used as it showed the best performance vs computational cost for the job. The geometry and mesh can be seen in Figures 21-24 as it was shown in chapter 4, their specific parameters, as well as the numerical setup, can be seen in Table 1-2.

The case was let to run for at least 13 cycles to allow the case to reach a stable periodical solution where disturbances created by the first interaction between the fluid domain and the

geometry (airfoil) at the beginning of the simulation could "wash out" downstream. The resultant power coefficient plot obtained is presented in Figure 37, where its periodicity can be appreciated as well as how the plot tends to convergence after a certain number of cycles. To measure this Figure 38 shows the convergence for the averaged power coefficient vs the cycles and it can be said that the values stay relatively constant after the fifth cycle. This is not always the case, as it was proven with the experimental study on chapter 4 where the use of more blades require more time to reach this convergence because of the greater interaction between the vortex shedding and the other blades.

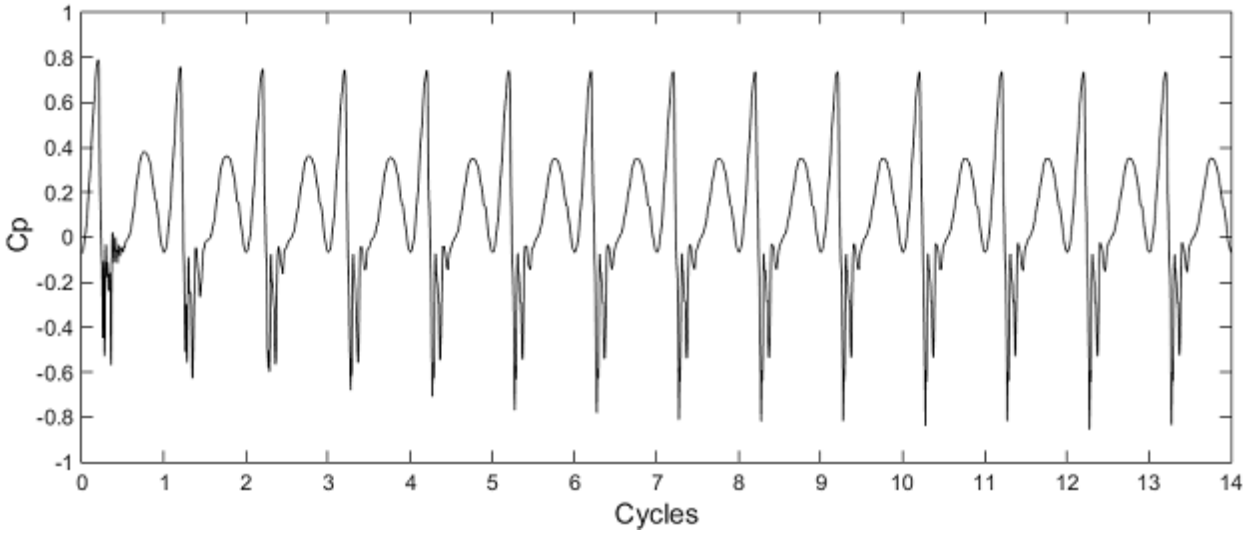

Figure 35- Power coefficient for fixed shape airfoil case.

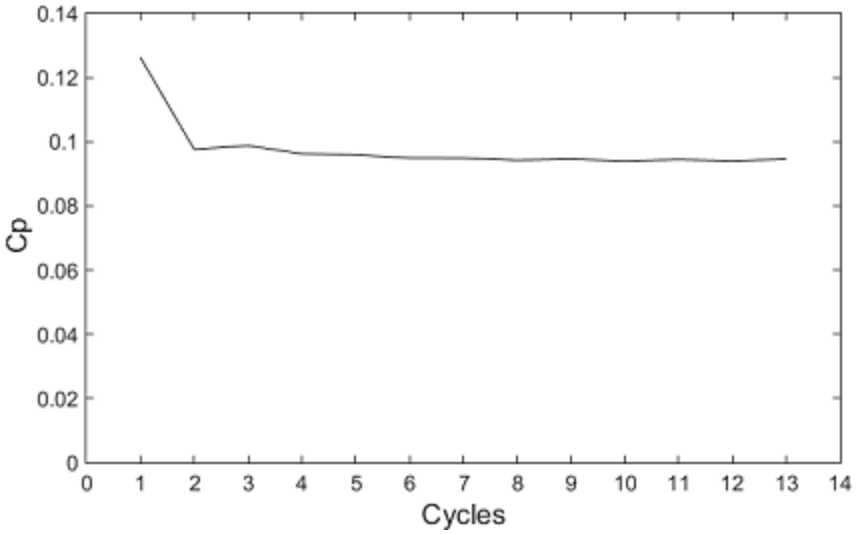

Figure 36- Convergence plot monitored by the power coefficient averaged.

To facilitate the analysis over the power coefficient plot, the last complete cycle is extracted and shown in Figure 39, this helps as a starting point to understand the flow's behavior over the airfoil and its surroundings. Initially, three regions can be identified on the graph, the first one being between the azimuthal angles 0 and 72 degrees where the power coefficient grows monotonically until it reaches its peak at a cp of 0.73 where suddenly drops. Hence entering the second region, this one characterized for an oscillating behavior and a negative power coefficient until reaching the 180 degrees azimuthal angle, this sudden drop is due to the dynamic stall and flow separation around the airfoil [21]. After reaching 180 degrees for the azimuthal angle, the power coefficient recovers and start being positive again with a more recovering growth, forming a local maximum in a smoother plateau-like a curve that peaks at around 270 degrees with a cp of 0.35, then it decreases at in a similar way until completing the cycle.

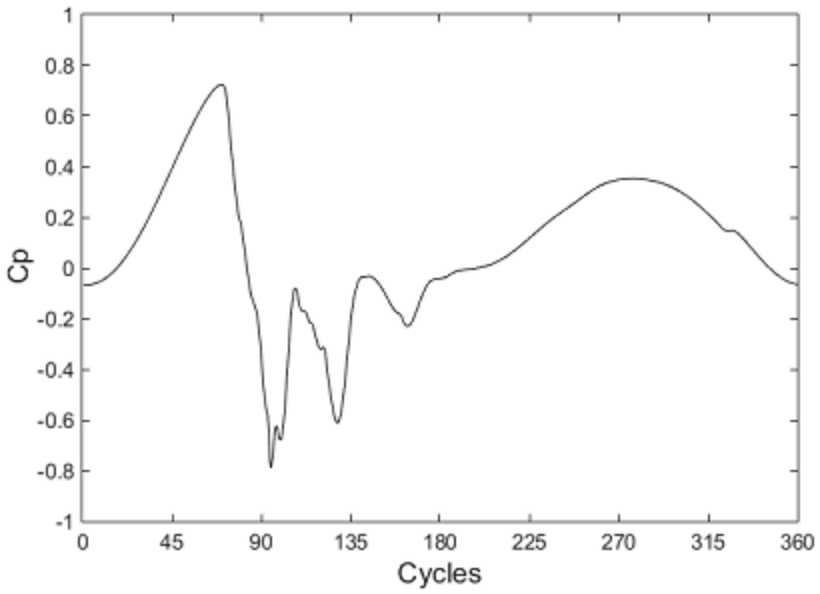

Figure 37-Last cycle plot from power coefficient for fixed shape airfoil case.

To start the characterization of the flow a series of scenes showing the vorticity, the turbulence viscosity ratio, as well as static pressure, was created, they all can be seen over Figures 42-47 and will be used in conjunction with lift and drag coefficient plots to explain the flow's behavior. The lift coefficient as seen in Figure 40 increases as expected over the first quadrant of motion between 0-70 degrees due to the increase in the effective angle of attack, which enhances the lift produced. The relation between the angle of attack and the azimuthal angle was established in Figure 9 and it was shown to be dependent on the TSR. In an analogous manner, the drag coefficient was plotted in Figure 41, it also presents a rapid increase in value over the first quadrant, explained by the increased angle of attack seen by the airfoil. This behavior is similar in an airfoil submitted to a pitch motion [18], where the drag and lift plots resemble those found on the static lift and drag curves for the first quadrant up to 70 degrees approximately. To see the flow over this region the contours plots in Figure 42 were created showing the turbulence viscosity ratio. The wake washing downstream can be appreciated after 13 cycles with a close-up

image of the airfoil, a static pressure scene it is also shown in Figure 43 where the pressure and suction side can be seen.

After 70 degrees the lift starts to oscillate rapidly maintaining this behavior for the whole second quadrant of movement, these sudden peaks and drops are signs of possible vortex generation with subsequent flow separation and shedding afterward, in other words, the dynamic stall is present. This can be appreciated in Figure 44 where the turbulent viscosity and vorticity are plotted to focus on the vortex development. This is supported by the results found by Vittecoq [61] where a dynamics stall analysis was conducted over a Darrieus type of VAWT, it was shown that the formation of the first vortex appears near the end of the first quadrant and its respective shedding occurs close to the beginning of the second quadrant for a TSR equal 3, which could be considered reasonably close to our 3.17 TSR. This leading-edge vortex will appear, grow and detach, moving over the airfoil surface, causing the maximum in drag observed in Figure 41 near the end of the first quadrant. As the vortex finally distance itself from the airfoil a sudden drop on the drag is observed, this could be due to the reattachment of the boundary layer. Figure 45 shows the static pressure of the airfoil and vortexes over the airfoil surface and near the trailing edge.

Finally for the third and fourth quadrant, Figure 40 shows that there is negative lift seen over the second half of the plot, this could be due to the negative angle of attack perceived by the blade when it stays on the second half of the cycle, but nonetheless the turbine still generates power around this area as seen on the power coefficient plot. In the case of the drag coefficient, this area it is stated by a positive "smooth" curve with an almost linear grow up to a local maximum where it plateaus around 270 degrees and a subsequent similar linear decrease until completing the cycle. Even though there is considerable vortex shedding occurring over the

second quadrant, and which vortexes can be seen more clearly moving downstream in Figure 46, they do not move fast enough to catch the same airfoil on the second part of the cycle. This can be seen in Figure 47 where the airfoil moves undisturbed by the vortex shedding, and especially in Figure 42 part "c" where the airfoil already started the cycle again by the time, the vortexes arrive at its path. This explains the "smoothness" of the lift and drags plots over these regions, nonetheless when more than one blade it is used these vortexes will interact with the other airfoils, at least if the same boundary and initial conditions were applied.

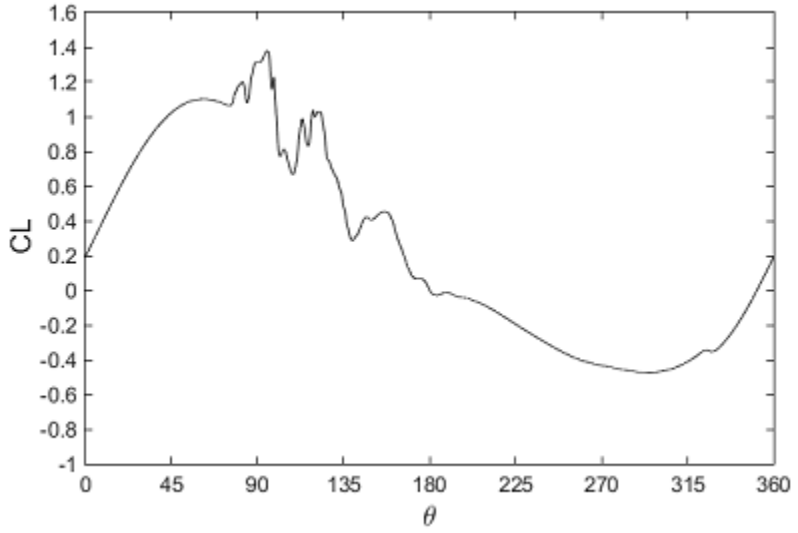

Figure 38- Lift coefficient for the fixed shape airfoil case.

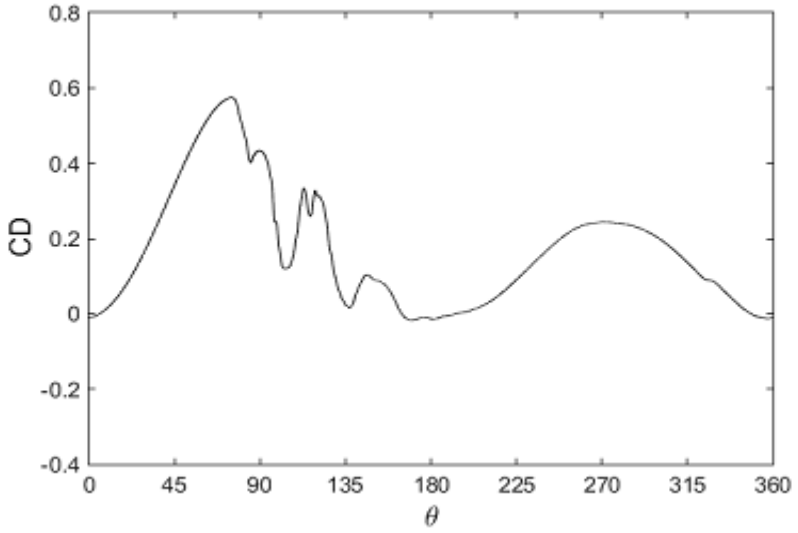

Figure 39- Drag coefficient for the fixed shape airfoil case.

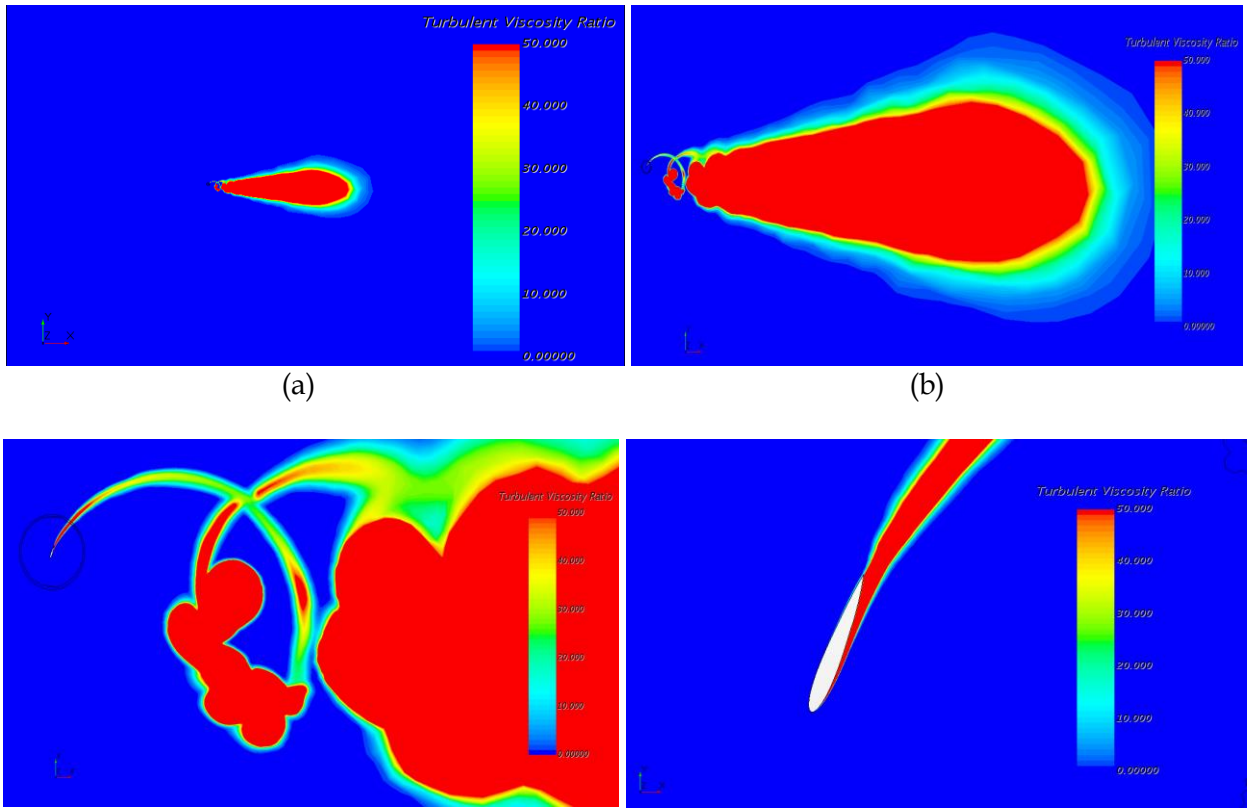

Figure 40- Turbulent viscosity ratio scenes for the fixed shape rotating airfoil inside the first quadrant showing: (a) Faraway view showing the entire domain. (b) Wake downstream of the turbine. (c) View over the rotating domain. (d) View over the airfoil.

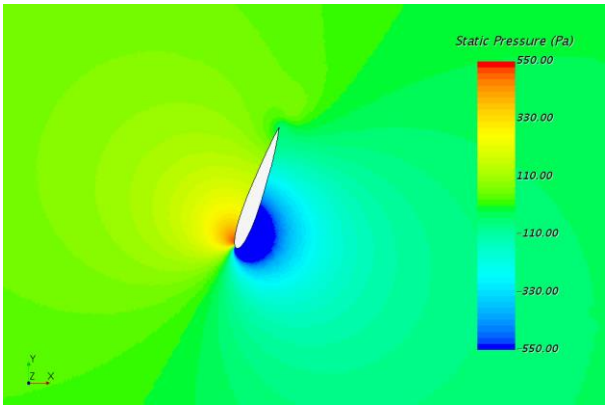

Figure 41- Static pressure scene over the airfoil inside the first quadrant.

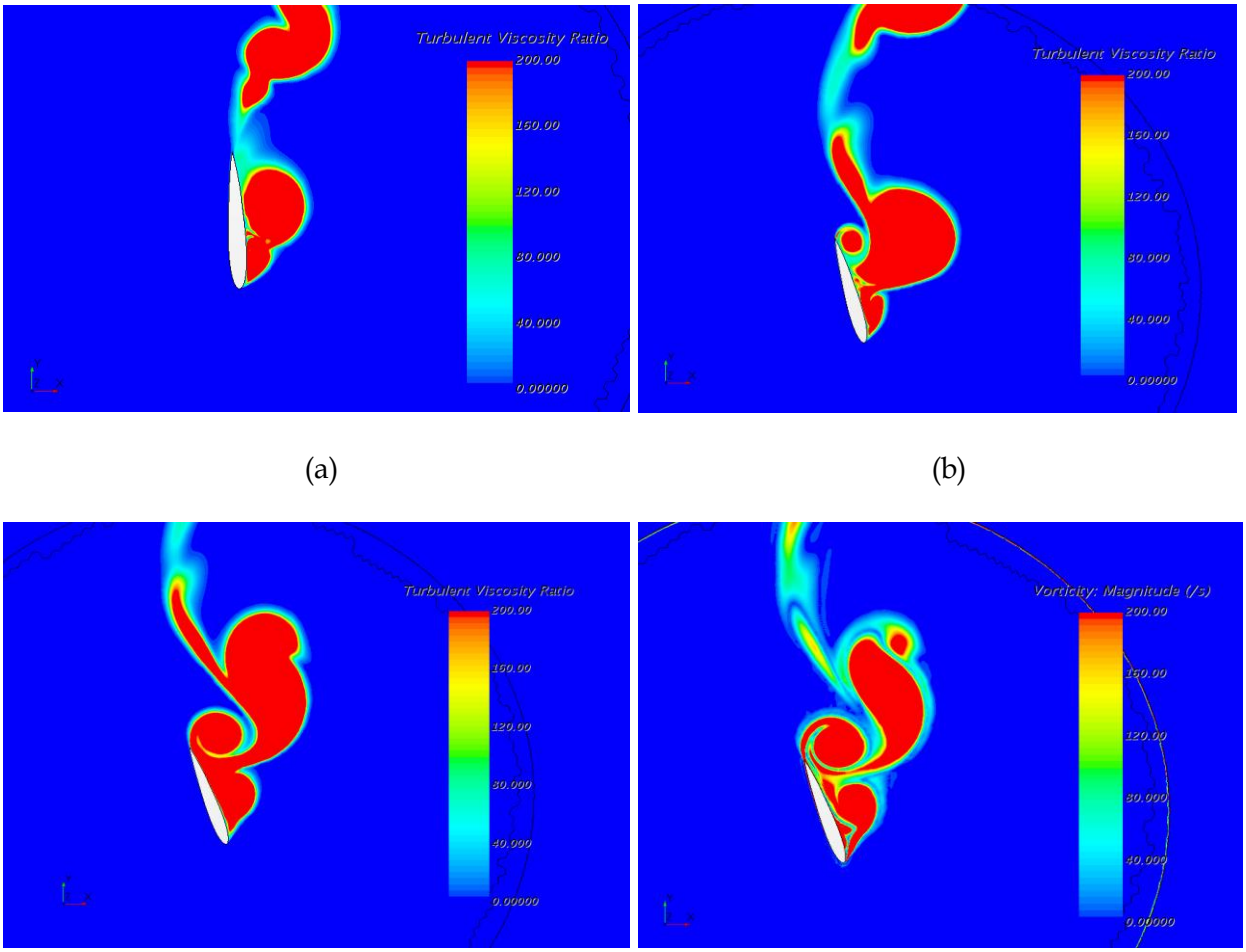

Figure 42- Turbulent viscosity ratio(a-c) and vorticity magnitude(d) scenes for the fixed shape rotating airfoil inside the second quadrant showing vortex generation, detachment and shedding over the airfoil.

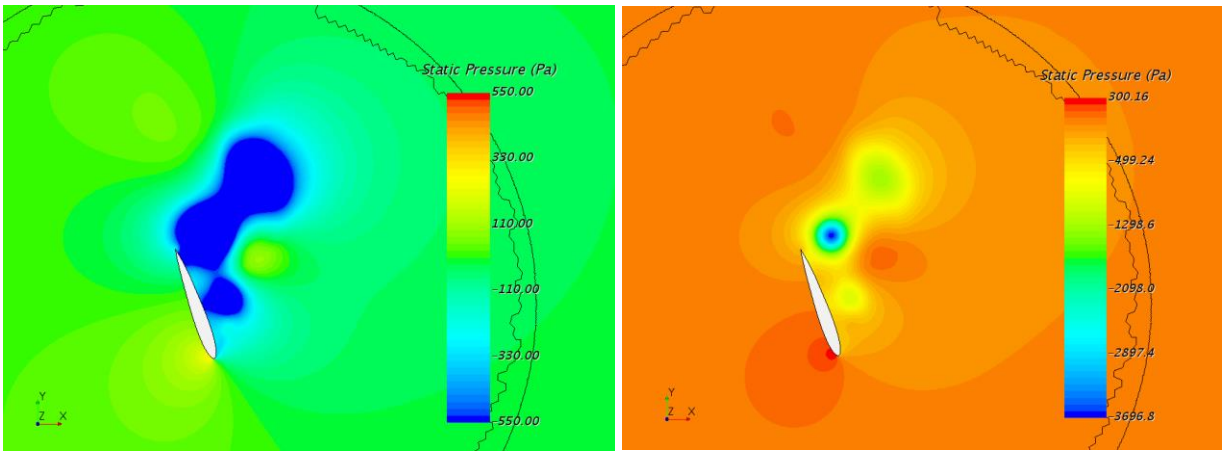

Figure 43- Static pressure scenes over the airfoil inside the second quadrant, vortexes are visible over the airfoil.

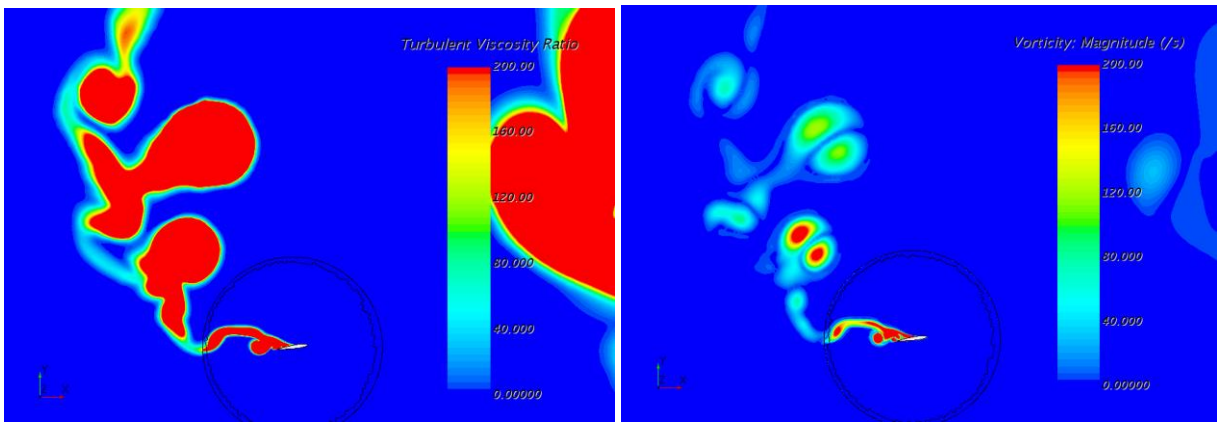

Figure 44- Comparison between turbulent viscosity ratio and vorticity magnitude for the fixed shape rotating airfoil at the beginning of the third quadrant.

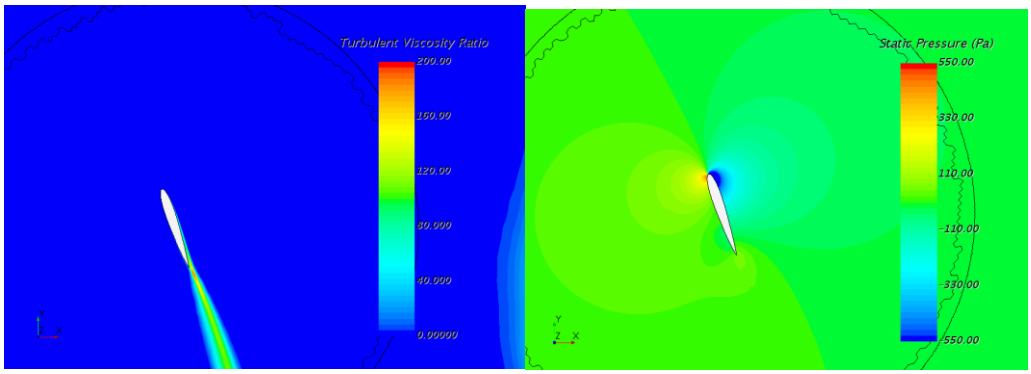

Figure 45- Comparison between turbulent viscosity ratio and static pressure for the fixed shape rotating airfoil over the fourth quadrant.

5.2. Fixed shape rotating airfoil – Inward case

The previous section established the baseline case using the "neutral" airfoil shape as seen on the bottom right corner of Figure 6, on this section and the next one however, we will focus on the two limiting shapes offered by the SSMA designed by Pankonien et al [16], as seen on the top left and right corners of Figure 6, these shapes will be known as Inward and Outward respectively, the description of said shapes by the use of approximate functions can be found in the work done by Tan [44]. By testing both cases we can analyze the maximum power coefficient reached by each shape, generate a plot comparing both to the baseline case and obtain a

maximum curve that will indicate where the deformation should be applied in order to maximize power.

The inward shaped airfoil started with the 1st cycle using the neutral shape airfoil positioned on the 90-degree azimuthal angle and activating simultaneously the rotational and morphing capabilities on Star CCM+© until the desired shape was obtained. This deformation step was used only at this stage for this case after the shape was obtained the morphing was deactivated for the rest of the simulation, Figure 48 shows a comparison between the before and after deforming the airfoil by using a static pressure plot. As a remainder the before the picture is the neutral shape which although similar to NACA0012 airfoil, is not completely symmetrical by itself, which explains the non-symmetry on the before pressure contour plot. After several cycles maintaining the inward shape on the airfoil the power coefficient is obtained and plotted in Figure 49 against the baseline scenario.

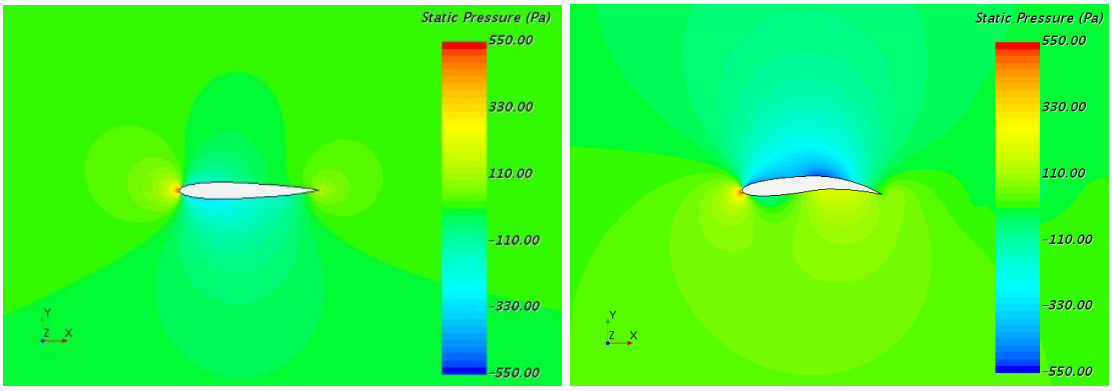

Figure 46- Before and after static pressure contour plot for the Inward case

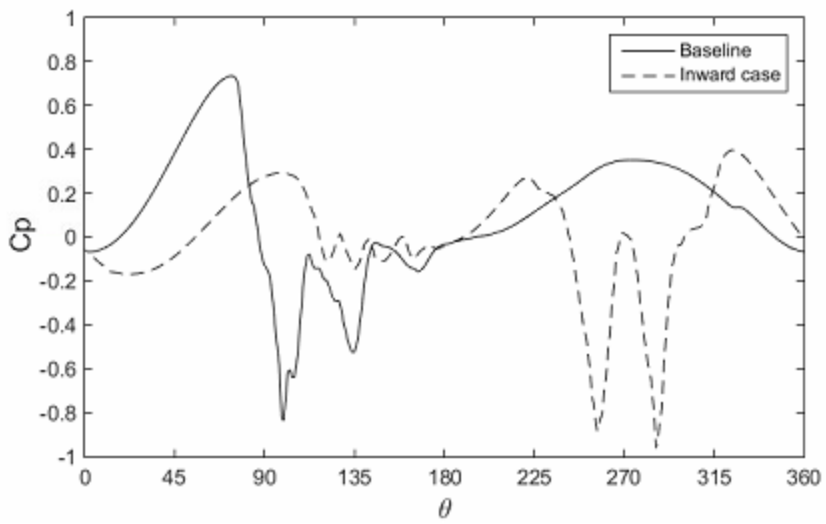

Figure 47- Power coefficient comparison between neutral and inward airfoil shapes.

By performing the same analysis as in the previous section, the power coefficient plot can be divided into four quadrants (90 degrees each) for its study. There are three important regions that can be highlighted inside the inward case, the first one being inside the first quadrant where the new shape has poor performance compared to the baseline case. This is related to the negative lift experienced by the new shape in this position on the cycle, and having a slowly recovering from there, as can be seen in Figure 50.

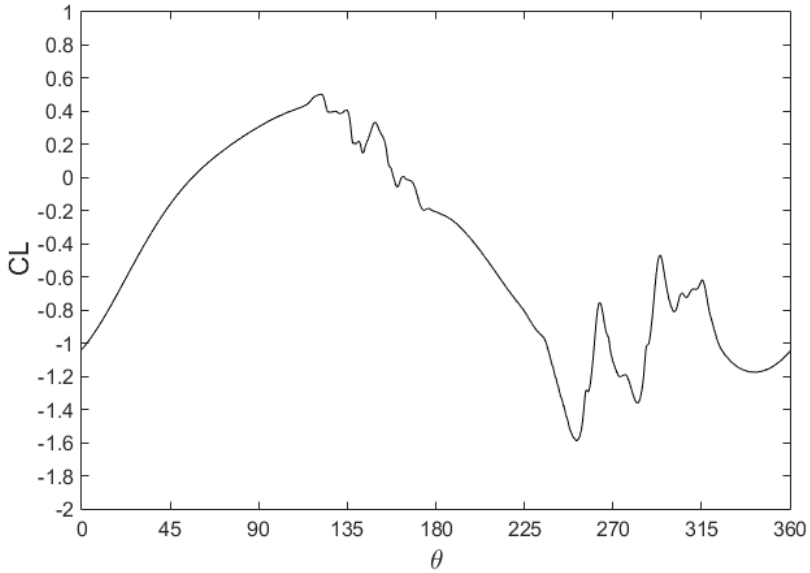

Figure 48- Normalized lift coefficient plot for the Inward case.

Perhaps the most important feature introduced by this shape is inside the second quadrant whereas seen in Figure 49, the negative power coefficient region mostly disappears besides some small negative peaks. This is considered of great importance as this region (inside the baseline case) represent the most problematic, where the dynamic stall is usually reached, and vortex shedding starts. Over this region, the vortexes appear to be attached longer and have less intensity than in the baseline case, Figure 51 helps visualize a pair of vortexes formed over the airfoil in this quadrant.

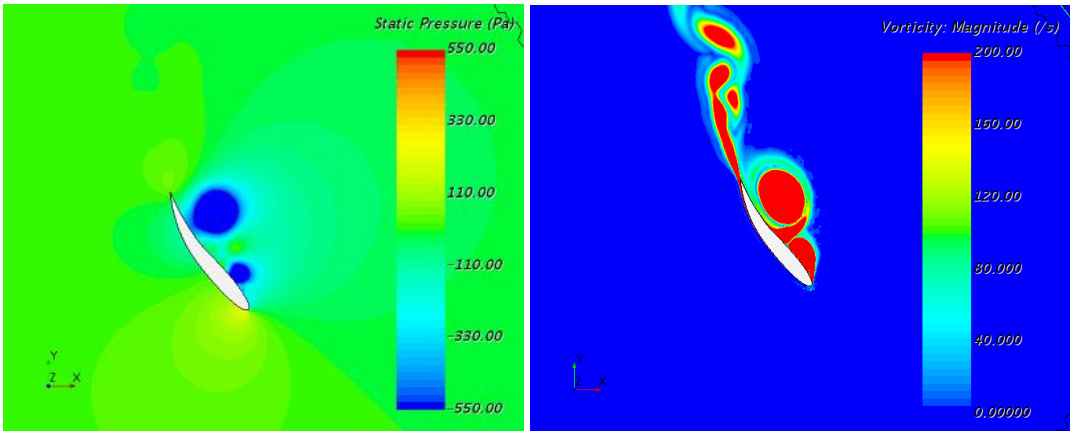

Figure 49- Static pressure (left) and Vorticity contour plots (right) for the inward case on the second quadrant showing vortexes over the airfoil.

Inside the third quadrant, the power coefficient grows slowly, but what it is more interesting here is that (as seen in Figure 52) the wake of vortices produced on the second quadrant develops and is visually much smaller than the one seen on Figure 46 for the baseline case.

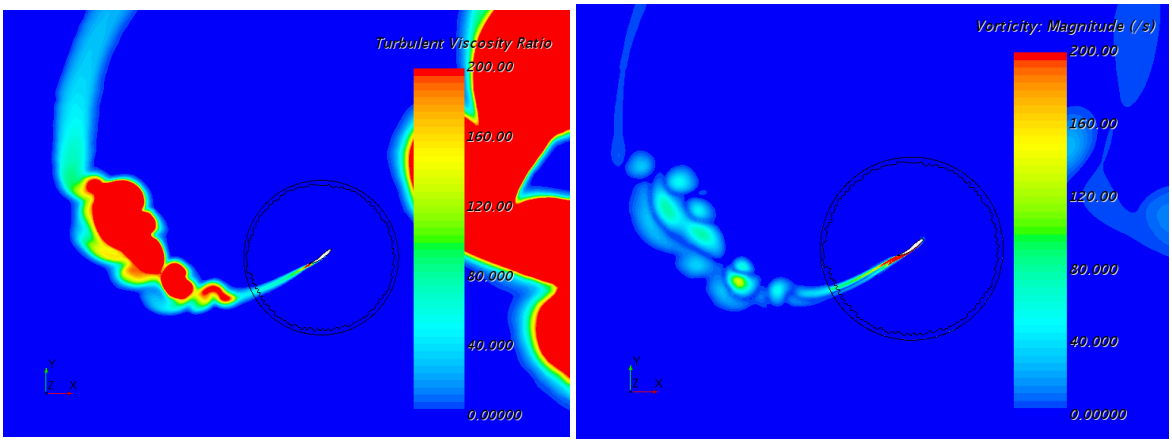

Figure 50- Turbulent viscosity ratio and vorticity contour plots for the Inward case on the third quadrant.

Finally, the third and fourth quadrants show high negative peaks in the power coefficient plot, which is mostly related to dynamic stall been reached over this region as can be noticed in Figure 53 where large vortexes are spotted shedding downstream. As a reference, Figure 54 shows the y+ values obtained after the deformation from neutral to inward shape over a histogram plot, as it can be noticed most values remain lower than y+ equal 1.

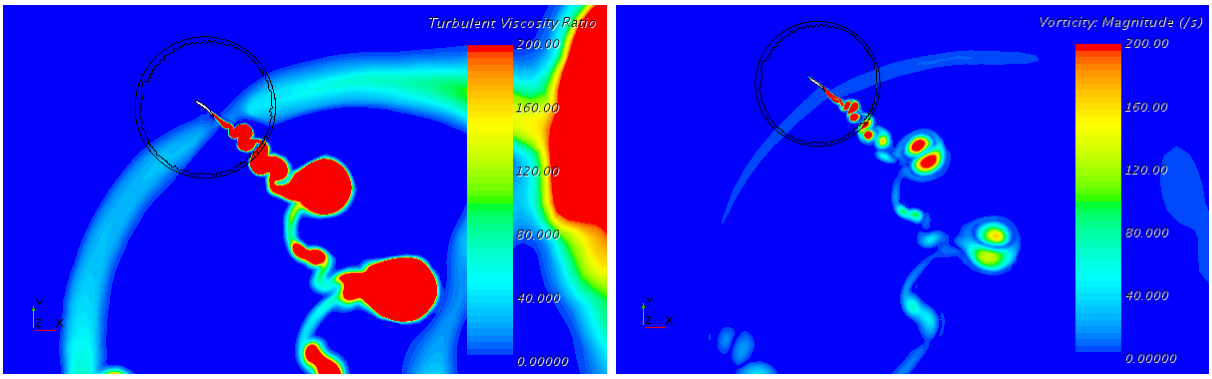

Figure 51- Turbulent Viscosity and vorticity contour plots for the Inward case on the fourth quadrant.

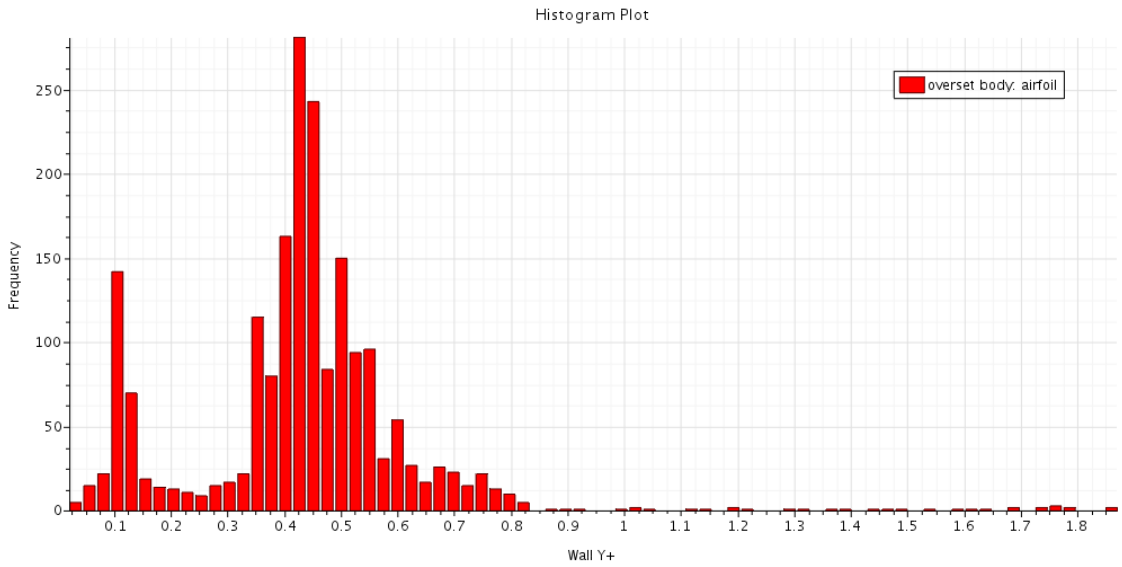

Figure 52- Histogram plot showing wall y+ value vs frequency for the inward case

5.3. Fixed shape rotating airfoil – Outward case

Following the same steps as the previous sections, now we explore the performance of the "outward" shape (seen at the top right of Figure 6) by using it across the whole cycle and tracking the power coefficient. Figure 55 shows a comparison using static pressure contour plots between the before/after morphing the airfoil from its neutral shape into the outward one.

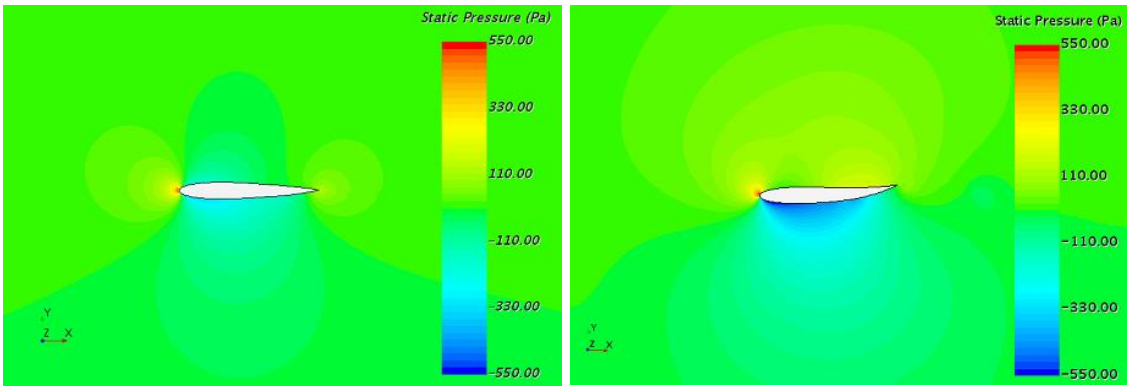

Figure 53-Before and after static pressure contour plot for the Outward case.

After running through several cycles, the power coefficient plot was generated, and it is shown on Figure 56 next to the baseline case, by comparing both results the outward shape

performed poorly in comparison to the neutral shape, with small regions where the power output is higher. By observing the second quadrant, this new shape affects negatively the dynamic stall by increasing its negative peaks, creating larger vortexes and a bigger wake, as it can be seen in Figure 57 with vorticity and turbulent viscosity plots.

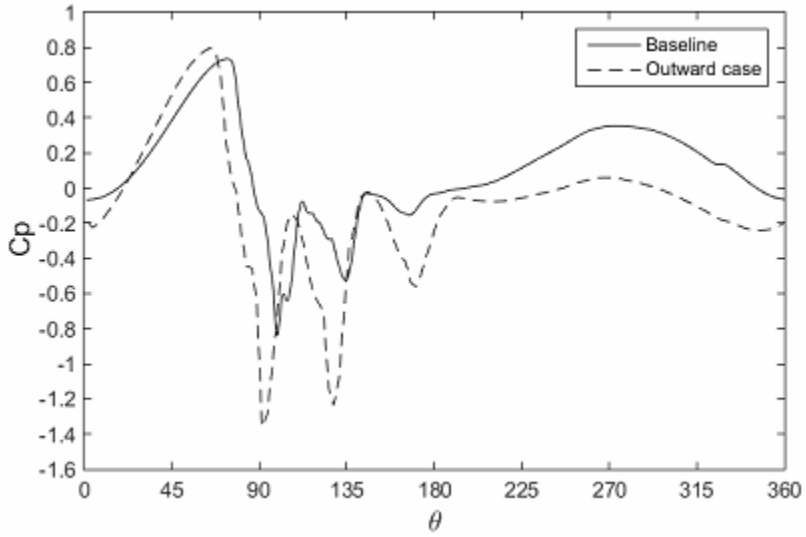

Figure 54-Power coefficient comparison between neutral and outward airfoil shapes.

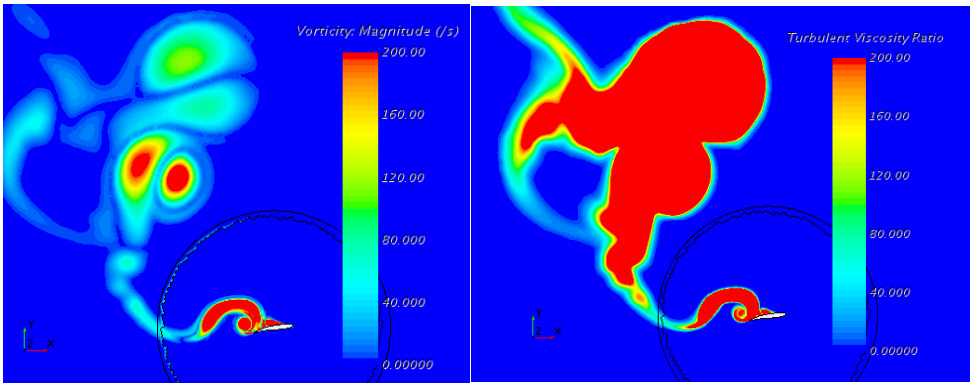

Figure 55- Turbulent viscosity ratio and vorticity contour plots for the Outward case on the third quadrant

With these results in mind, it is considered that the outward shape is not a suitable candidate to be used in this case for the specific conditions of our study. Although it needs to be pointed out that STAR CCM+© did not allow for the full outward shape (as shown in Figure 6)

to be reached, as negative elements start to appear near the trailing edge, subsequently stopping the simulation, therefore the morphing capabilities had to be stopped before reaching the final shape. Re-meshing was not considered to be a viable option as the goal was to obtain a more continuous simulation, and remeshing would have made the case more costly as if introduced on the final case, it would have to be re-meshed not only to reach the outward case but also when coming back from it to the neutral shape again, per cycle. Finally, Figure 58 shows a histogram plot with the +y values for the outward case, showing that mostly they have values lower than 1.

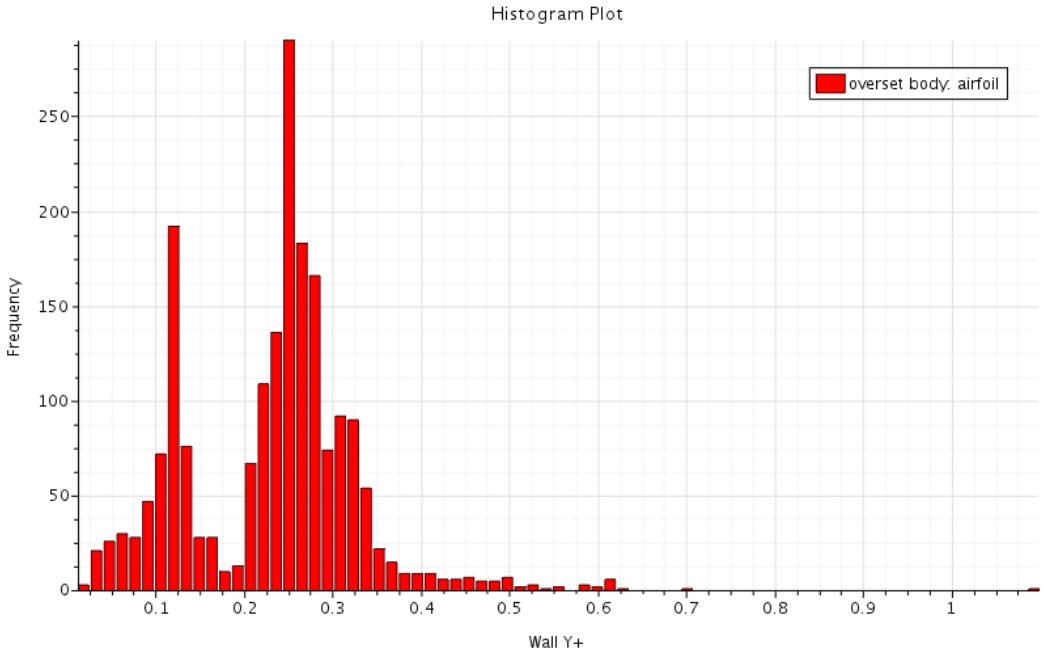

Figure 56- Histogram plot showing wall y+ value vs frequency for the outward case

5.4. Morphed airfoil

Once the three main airfoil shapes have been tested (neutral, inward and outward), it is time to consider how an optimal cycle would look like and what it is achievable with the tools available. First, we need to compare the three shapes by using the power coefficient plots obtained in previous sections, this is done in Figure 59. Then the maximum values can be

extracted and plotted in Figure 60, where it can be argued that the mayor gained offered by the non-neutral shapes belongs to the inward case, especially the area covered by the second quadrant where a series of negative peaks caused by dynamic stall is minimized.

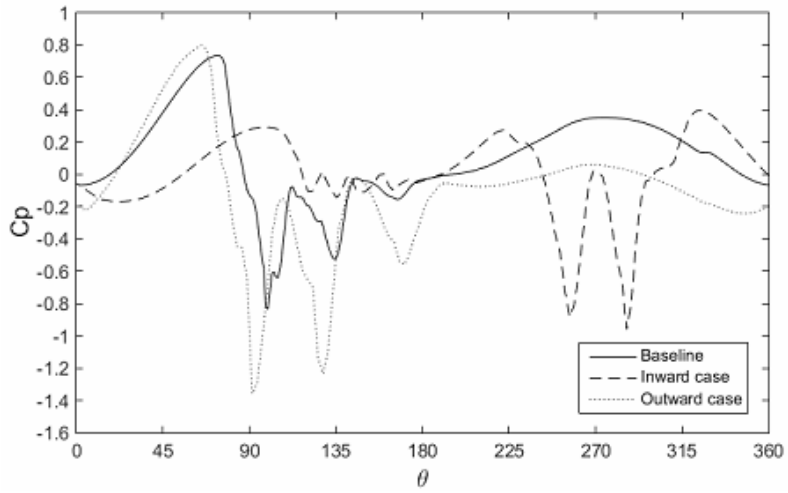

Figure 57- Power coefficient comparison between neutral, inward and outward airfoil shapes.

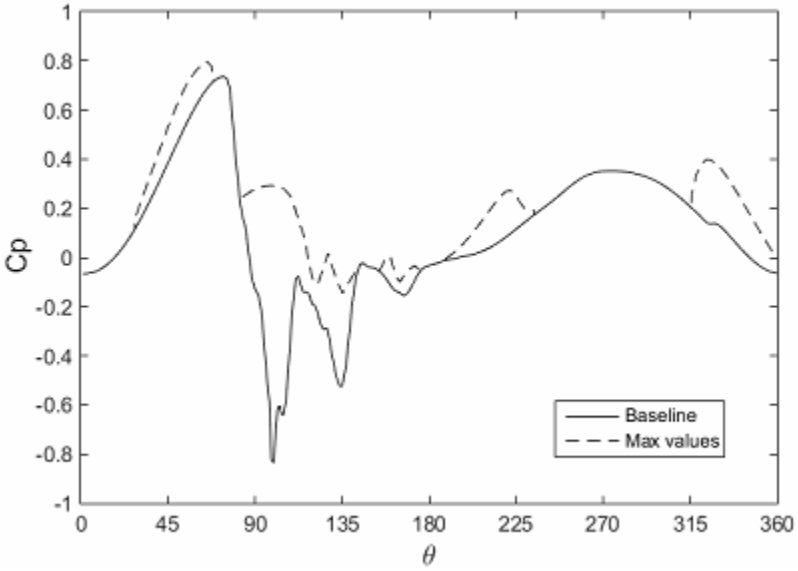

Figure 58- Power coefficient comparison between maximum values for fixed shapes and baseline case.

As such, the inward shape will be added to the final morphing case over this quadrant, although this shape starts to perform better than the baseline case at approximately 82º on the cycle, it will be implemented starting from 90º because of the difficulties found to implement

both morphing and rotational motion simultaneously on STAR CCM+©. The easiest way found in this study was to transition from one shape into the other during brief periods of time over the positions 0^o, 90^o, 180^o and 270^o for the azimuthal angles, when other locations where tried the morphing became hard to control and the airfoil lost its shape quickly, with negative cells being generated. Regarding this issue, the other gains obtained over quadrants 1,3 and 4 by the outward and inward shapes are too small or they are be located over regions difficult to reach by the current technique, where a smooth transition wouldn't be possible. Therefore, a final case was established, it is composed mainly of the neutral shape encompassing the 1st, 3rd, and 4th quadrant, and by the inward shape over the 2nd quadrant, the power coefficient obtained by this case it is showed on Figure 61.

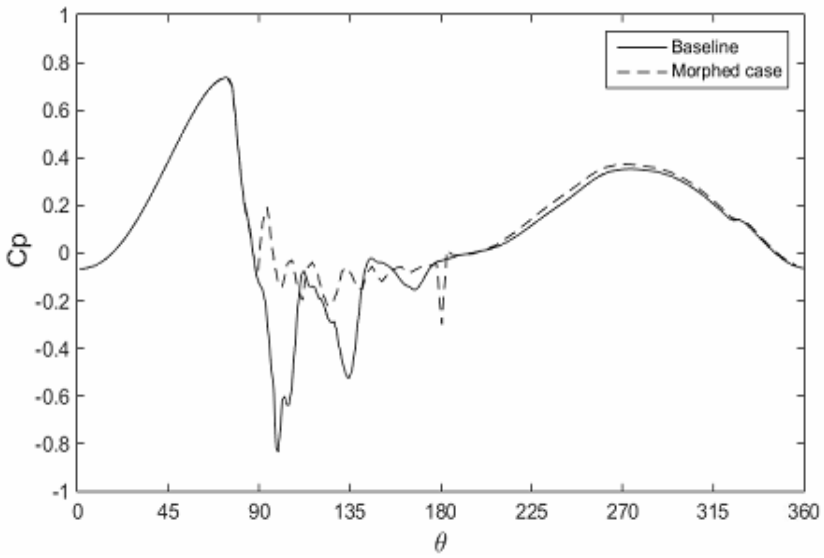

Figure 59- Power coefficient comparison between the morphed airfoil and the baseline case.

In can be noticed by Figure 61 that even though the negative area over the second quadrant was reduced, its magnitude is much smaller than the positive values that were obtained previously when only the inward shape was used. This could be due to the fact that by maintaining the same inward shape through the first quadrant into the second one, caused the

vortexes to remained attached to the airfoil as the transition between the effective angles of attack is only due to the rotation, and therefore smoother than for the morphed case. Such is the case that when the morphing is applied at 90^o a small positive peak appears on the plot, however, there's a subsequent oscillation during the rest of the second quadrant. This is attributed to a chain of small vortexes that are continuously generated as evidenced in Figure 62, until the case transitions back into the neutral shape at 180^o where a final peak is observed.

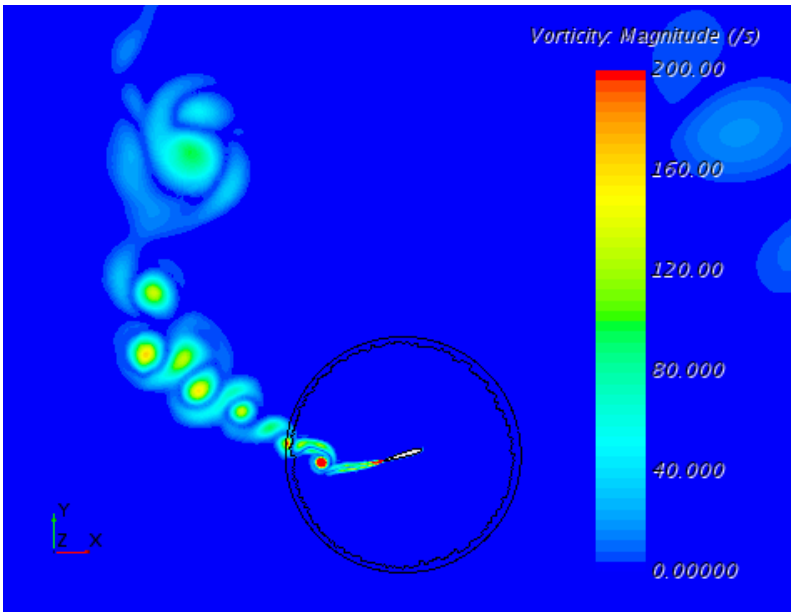

Figure 60- Vorticity contour showing vortexes being shredded by the morphed airfoil.

Finally, in order to compare the performance between all cases, Table 7 shows the averaged value for the power coefficients. It can be seen how on average, the inward case power output is almost 0, and the outward one is negative, meaning that will consume energy to be able to maintain the same rotation as in the simulation. Lastly, the final morphed case registers an improvement of 46.2% in the power coefficient when compared to the baseline.

Table 6- Comparison between averaged power coefficient values for all cases.

Case	Baseline	Inward	Outward	Maximum	Morphed
Cp	0.09608	-0.00074	-0.10785	0.21533	0.14045

6. Conclusions and future work

The main purpose of this work is to study the performance of a simulated VAWT with and without using morphing capabilities applied to its blades. This is archived by implementing the said features inside the STAR CCM+© software package. To archive this, a methodology is developed by creating a series of verification cases that are tested against a benchmark scenario backed by experimental data, as well as grid and time step sensitivity tests. The results obtained for the verifications cases are sufficiently accurate and showed satisfactory convergence for finer meshes and a smaller time step. Furthermore, the comparison between experimental data and our simulated benchmark case showed good agreement between most values for the non-dimensionalized normal and tangential forces.

Three cases are created to investigate the rotating airfoil of a VAWT, one "normal" case representing an approximate NACA 0012 airfoil used as a base scenario and two maximum deformation cases, known as inward and outward. The study of these cases highlighted the areas where the presence of dynamic stall and vortex shedding are higher, as well as showing the effects that cambering the airfoil (for the inward and outward configurations) has over the power coefficient. The baseline case shows that the second quadrant of motion (starting at an azimuthal angle equal to 90 degrees) has the greatest loss in power coefficient with a highly variable and negative zone, which has been shown to be related to the development of dynamic stall and shedding vortexes over the region. By comparing the three cases a maximum power coefficient plot is created, which represents the maximum power reachable through morphing the airfoils.

Finally, both rotation and deforming motions are used simultaneously on an optimized case, where deformation was applied during the second quadrant by changing the shape of the airfoil from base to the "inward" case. This resulted in an increase of 46,2% of the overall power

coefficient by greatly reducing the dynamic stall intensity, which is also confirmed qualitatively by using vorticity counter plots where the size of the vortexes shed is much smaller than those of the baseline case. This demonstrates that deforming an airfoil over certain regions in a VAWT path can yield great gains in power output, as well as proving the feasibility of simulating both rotation and deformation simultaneously within STAR CCM+©.

More work is still needed, as 2D simulations lack the effects of 3D structures (both by the geometry and the flow itself), which may affect the power coefficient and levels of dynamic stall encounter. In this work, only one blade was investigated for a specific size of a small turbine. The next step would be to investigate this technology for large VAWTs and assess the potential to increase the coefficient of power. Finally, it is suggested that a multivariable analysis should be done, where the power coefficient is optimized by morphing the blades at specific instances.

Bibliography

[1] Aklin M., Urpelainen J. (2018). Renewables: The Politics of a Global Energy Transition, The MIT Press.

[2] Ryoichi H. (2016) Prediction of wind power generation output and network operation. Chapter 5. Integration of Distributed Energy Resources in Power Systems. Implementation, Operation and Control. Pages 109-131. Academic Press.

[3] Wynn, G. (2018). IEEFA Update: A renewable Energy Revolution in Uruguay for All the World to See. Institute for Energy Economics and Financial Analysis. Retrieved from http://ieefa.org/ieefa-update-a-renewable-energy-revolution-in-uruguay-for-all-the-world-to-see/

[4] Wynn, G. (2018). IEEFA Latin America: Uruguay nears world-leading market share for variable renewables. Institute for Energy Economics and Financial Analysis. Retrieved from http://ieefa.org/ieefa-latin-america-uruguay-nears-world-leading-market-share-for-variable-renewables/

[5] Meinshausen, M., Meinshausen, N., Hare, W., Raper C. B. S., Frieler, K., Knutti, R. , Frame, D. J., Allen, M. R. (2009). Greenhouse-gas emission targets for limiting global warming to 2 °C. Nature, 458, 1158-1162.

[6] Oyhenard, A. (2017, May 8). Aerogenerador tiene área de «barrido» superior a una cancha de fútbol. El observador Newspaper. Retrieved from http://marcapaisuruguay.gub.uy/aerogenerador-area-barrido-superior-una-cancha-futbol-desarrollador-aleman-parques-eolicos-sowitec-inicio-la-fase-pruebas-uruguay-una-granja-eolica-flores-492-meg/

[7] Möllerström, E., Gipe, P., Beurskens, J., Ottermo, F. (2019). A historical review of vertical axis wind turbines rated 100 kW and above. Renewable and Sustainable Energy Reviews, Volume 105, 1-13. https://doi.org/10.1016/j.rser.2018.12.022

[8] Eriksson, S., Bernhoff, H., Leijon, M. (2008). Evaluation of different turbine concepts for wind power. Renewable and Sustainable Energy Reviews, 12:1419–1434.

[9] Hau, E. (2000). Wind turbines: fundamentals, technologies, application, economics. DOI: 10.1007/3-540-29284-5

[10] Betz, A. (1966). Introduction to the theory of flow machines. 1st Edition, Pergamon Press. https://doi.org/10.1016/C2013-0-05426-6

[11] Amet, E., Maitre, T., Pellone, C., Achard, J. L. (2009). 2d numerical simulations of blade vortex interaction in a darrieus turbine. Journal of fluids engineering, 131(11): 111103 (15 pages).

[12] Secanell, M., Suleman, A., Gamboa, P. (2006). Design of a morphing airfoil using aerodynamic shape optimization. AIAA Journal, 44(7):1550–1562.

[13] Kerho, M. (2007) Adaptive airfoil dynamic stall control. Journal of Aircraft, 44(4):1350–1360.

[14] Hefeng, D., Chenxi, W., Shaobin, L., Xi Zhen, S. (2015). Numerical research on segmented flexible airfoils considering fluid-structure interaction. Procedia Engineering, 99:57–66.

[15] Anderson, J. D. (2010). Fundamentals of aerodynamics, 5th edition, McGraw-Hill Education.

[16] Pankonien, A., Faria, C., Inman, D. (2013). Synergistic smart morphing aileron. 54th AIAA/ASME/ASCE/AHS/ASC Structures, Structural Dynamics, and Materials Conference, Boston.

[17] Bhutan, S., Biswas, A. (2014). Investigations on self-starting and performance characteristics of simple H and hybrid H-Savonius vertical axis wind rotors, Energy Conversion and Management, Volume 87, 859-867.

[18] Geissler, W., Van der Wall, B. (2017). Dynamic stall control on flapping wing airfoils. Aerospace Science and Technology, 62:1-10.

[19] Gosselin, R., Dumas, G., Boudreau, M. (2013). Parametric study of H-darrieus vertical-axis turbines using uRANS simulations, Paper CFDSC-2013, 178: 6–9.

[20] Munson, B., Young, D., Okiishi, T. (2002). Fundamentals of Fluid Mechanics. 4th edition, John Wiley and Sons, Hoboken.

[21] Magri, L., Galvanetto, U. (2012). Example of a non-smooth Hopf bifurcation in an aeroelastic system. Mechanics Research Communications, 40:26–33

[22] McCroskey W. J. (1981). The phenomenon of dynamic stall. Technical report, National Aeronautics and Space Administration Moffett Field, CA Ames Research Center.

[23] McCroskey, W., Carr, L., McAlister, K. (1976) Dynamic stall experiments on oscillating airfoils. AIAA Journal, 14(1):57–63.

[24] Mulleners, K., Raffel, M. (2013). Dynamic stall development. Experiments in Fluids, 54:1–9.

[25] Lee, T., Gerontakos, P. (2004) Investigation of flow over an oscillating airfoil. Journal of Fluid Mechanics, 512:313-341, Cambridge University Press.

[26] Ferreira, C. J. S., Van Zuijlen, A., Bijl, H., Van Bussel, G., Van Kuik, G. (2010). Simulating dynamic stall in a two-dimensional vertical-axis wind turbine: verification and validation with particle image velocimetry data. Wind Energy. 13(1):1–17.

[27] Ferreira, C. J. S., van Kuik, G. A. M., van Bussel, G. J. W., Scarano, F. (2009). Visualization by PIV of dynamic stall on a vertical axis wind turbine. Experiments in Fluids, 46(1):97-108. DOI: 10.1007/s00348-008- 0543-z

[28] Corcos, G., Sherman, F. (1984). The mixing layer: deterministic models of a turbulent flow. Part 1. Introduction and the two-dimensional flow. Journal of Fluid Mechanics, 139:29–65.

[29] Fujisawa, N., Shibuya, S. (2001). Observations of dynamic stall on darrieus wind turbine blades. Journal of Wind Engineering and Industrial Aerodynamics, 89(2):201–214.

[30] Choudhry, A., Leknys, R., Arjomandi, M., Kelso, R. (2014). An insight into the dynamic stall lift characteristics. Experimental Thermal and Fluid Science, 58:188– 208.

[31] Scheurich, F. (2011). Modelling the aerodynamics of vertical-axis wind turbines. PhD thesis, University of Glasgow.

[32] Ansys. (2013). Ansys Fluent User Guide, release 15.0, ANSYS Fluent.

[33] Komeili, M. (2016). Large Eddy Simulation of Vertical Axis Wind Turbine for Low Reynolds Number Applications. PhD thesis. Concordia University. Montreal.

[34] Batina, J. T. (1990). Unsteady Euler airfoil solutions using unstructured dynamic meshes. AIAA journal. 28(8): 1381–1388

[35] Blom, F. J. (2000). Considerations on the spring analogy. International Journal for Numerical Methods in Fluids. 32(6): 647–668.

[36] Samareh, J. A. (2001). Survey of shape parameterization techniques for high-fidelity multidisciplinary shape optimization. AIAA journal, 39(5):877–884.

[37] Degand, C., Farhat, C. (2002). A three-dimensional torsional spring analogy method for unstructured dynamic meshes. Computers & structures, 80(3): 305–316.

[38] Bottasso, C. L., Detomi, D., Serra, R. (2005). The ball-vertex method: a new simple spring analogy method for unstructured dynamic meshes. Computer Methods in Applied Mechanics and Engineering, 194(39):4244–4264.

[39] Löhner, R., Yang, C., Onate, E. (1998). Viscous free surface hydrodynamics using unstructured grids. Proceedings of the 22nd symposium on naval hydrodynamics, 476–490.

[40] Hsu, S. -Y., Chang, C. -L., Samareh, J. (2012). A Simplified Mesh Deformation Method Using Commercial Structural Analysis Software. NASA Langley Research Center Hampton, 10th AIAA/ISSMO Multidisciplinary Analysis and Optimization Conference. pp 32.

[41] De Boer, A., Van der Schoot, M., Bijl, H. (2007) Mesh deformation based on radial basis function interpolations. Computers and Structures, 85(11-14):784–795.

[42] Bos, F., Van Oudheusden, B., Bijl, H. (2013). Radial basis function-based mesh deformation applied to simulation of flow around flapping wings. Computers and Fluids, 79:167–177.

[43] Su, X., Sheng, C., Allen, C. (2011). An Efficient Mesh Deformation Approach Based on Radial Basis Functions in an Unstructured Flow Solver. 20th AIAA Computational Fluid Dynamics Conference. pp 17.

[44] Tan, J. (2017). Simulation of morphing blades for vertical axis wind turbines. Master Dissertation. Concordia University.

[45] Siemens. (2017). STAR CCM+ User manual. Version 12.06.011. Siemens PLM Software.

[46] Taylor, L. (2018). Large eddy simulation of oscillating and deforming airfoils. Master dissertation. Concordia University

[47] Celik, I. (2003). RANS/LES/DES/DNS: The Future Prospects of Turbulence Modeling. Journal of Fluids Engineering. 127(5): 829-830. https://doi.org/10.1115/1.2033011

[48] Zhiyin, Y. (2015). Large-eddy simulation: Past, present and the future. Chinese Journal of Aeronautics. 28(1): 11-24.

[49] Wagner C., Shishkin A., Shishkina O. (2011) The use of Direct Numerical Simulations for solving industrial flow problems. Direct and Large-Eddy Simulation VIII. ERCOFTAC Series, vol 15. Springer, Dordrecht.

[50] Zhou, Q., Fan, L. -S. (2015). Direct numerical simulation of low-Reynolds-number flow past arrays of rotating spheres. Journal of Fluid Mechanics. 765:396-423. DOI: 10.1017/jfm.2014.732

[51] Bakker, A. (2008). Lecture 10 – Turbulence Models. Applied Computational Fluid Dynamics course. Retrieved from: http://www.bakker.org/dartmouth06/engs150/10-rans.pdf

[52] Wilcox, C. D. (2006). Turbulence Modeling for CFD. 3rd Edition. D C W Industries.

[53] McLean, D. (2017). Development of the Dual-Vertical-Axis wind turbine with active blade pitch control. Master dissertation. Concordia University.

[54] Anderson, J., Wendt, J. E. (2009). Computational Fluid Dynamics: An Introduction. 3rd edition. Springer.

[55] Cable, M. (2009). An Evaluation of Turbulence Models for the Numerical Study of Forced and Natural Convective Flow in Atria. Master dissertation. Queen's University.

[56] Menter, F.R. (1994). Two-equation eddy-viscosity turbulence modeling for engineering applications. AIAA Journal. 32(8):1598-1605.

[57] Schlichting, H., Gersten, K. (2000). Boundary-Layer Theory. 8th edition. Springer.

[58] Ferziger, J. H., Peric, M. (2002). Computational methods for fluid dynamics. 3rd edition. Springer

[59] Pletcher, R. H., Tannehill, J. C., Anderson, D. (2012). Computational fluid mechanics and heat transfer. CRC Press.

[60] Castelein, D. (2015). Dynamic stall on vertical axis wind turbines: creating a benchmark of Vertical Axis Wind Turbines in Dynamic Stall for validating numerical models. Master dissertation. Delft University of Technology.

[61] Laneville, A., Vittecoq, P. (1986). Dynamic stall: the case of the vertical axis wind turbine. Journal of Solar Energy Engineering. 108(2):140-145. DOI: 10.1115/1.3268081